

# Evidence for Misalignment Between Debris Disks and Their Host Stars

SPENCER A. HURT<sup>1,2</sup> AND MEREDITH A. MACGREGOR<sup>2</sup>

<sup>1</sup>*Department of Physics and Astronomy, University of Wyoming, Laramie, WY 82071, USA*

<sup>2</sup>*Department of Astrophysical and Planetary Sciences, University of Colorado, Boulder, CO 80309, USA*

## ABSTRACT

We place lower limits on the obliquities between debris disks and their host stars for 31 systems by comparing their disk and stellar inclinations. While previous studies did not find evidence for misalignment, we identify 6 systems with minimum obliquities falling between  $\sim 30^\circ - 60^\circ$ , indicating that debris disks can be significantly misaligned with their stars. These high-obliquity systems span a wide range of stellar parameters with spectral types K through A. Previous works have argued that stars with masses below  $1.2 M_\odot$  (spectral types of  $\sim$ F6) have magnetic fields strong enough to realign their rotation axes with the surrounding disk via magnetic warping; given that we observe high obliquities for relatively low-mass stars, magnetic warping alone is likely not responsible for the observed misalignment. Yet, chaotic accretion is expected to result in misalignments of  $\sim 20^\circ$  at most and cannot explain the larger obliquities found in this work. While it remains unclear how primordial misalignment might occur and what role it plays in determining the spin-orbit alignment of planets, future work expanding this sample is critical towards understanding the mechanisms that shape these high-obliquity systems.

## 1. INTRODUCTION

The Sun’s equatorial plane is well-aligned with the ecliptic, having an obliquity of  $7.155 \pm 0.002^\circ$  (Beck & Giles 2005). Most of the major solar system bodies move in nearly the same plane, suggesting that the planets formed from a protoplanetary disk that was rotating in the same direction as the early Sun. It has commonly been thought that other planetary systems form similarly and that exoplanet orbital axes should be closely aligned with their stars’ spin axes. However, observational techniques such as the Rossiter-McLaughlin effect (Queloz et al. 2000; Shporer & Brown 2011; Triaud 2018), Doppler shadows (Albrecht et al. 2007; Zhou et al. 2016), and gravity darkened transits (Barnes 2009; Ahlers et al. 2020) have measured large spin-orbit angles for many extra-solar systems (Albrecht et al. 2022).

Possible mechanisms responsible for spin-orbit misalignment generally fall into three categories: primordial misalignment, post-formation misalignment, and changes in the stellar spin axis that are independent of planet formation. The first, primordial misalignment, suggests that a protoplanetary disk is misaligned with its star’s rotation axis and that planets with large spin-orbit angles form in situ. Processes that could misalign the disk include chaotic accretion (where the late arrival of material from the molecular cloud warps or tilts the disk; Bate et al. 2010; Thies et al. 2011; Fielding et al. 2015; Bate 2018; Takaishi et al. 2020), magnetic warping (when the Lorentz force between a young star and ionized inner disk magnifies any initial misalignments; Lai et al. 2011; Foucart & Lai 2011), and secular processes involving an inclined stellar or planetary companion (Borderies et al. 1984; Lubow & Ogilvie 2000; Batygin 2012; Matsakos & Königl 2017). Post-formation misalignment implies that after formation, gravitational interactions alter a planet’s orbit. This could occur via planet-planet scattering (Malmberg et al. 2011; Beaugé & Nesvorný 2012) or secular processes like Kozai-Lidov cycles (Naoz 2016) or disk-driven resonance (Petrovich et al. 2020). Both primordial and post-formation misalignment could also occur via stellar clustering, which appears to have a strong influence on the architecture of planetary systems (Tristan & Isella 2019; Winter et al. 2020; Rodet & Lai 2022) and may be commonplace (Yep & White 2022). Thirdly, it has been proposed that stars with convective cores and radiative envelopes can reorient themselves without an external torque due to internal gravity waves generated at the radiative-convective boundary (Rogers et al. 2012, 2013).

Hot Jupiters—massive planets on very short orbits—frequently appear misaligned with hot, rapidly-rotating stars that generally fall above the Kraft break ( $\sim 6200$  K; Kraft 1967) while low-mass planets appear misaligned with both cool and hot stars (Winn et al. 2010; Schlaufman 2010; Albrecht et al. 2022). It has been suggested that hot Jupiters first enter high-obliquity orbits regardless of their host stars’ properties; however, tidal interactions between

the massive, close-orbiting planets and the relatively thick convective envelopes found in stars below the Kraft break realign the stellar spin axes with the hot Jupiters' orbits. The mechanisms responsible for spin-orbit misalignment may help reveal how these exotic planets form. While formation in situ through core accretion may be possible (Batygin et al. 2016), it would be challenging for enough material to accumulate and develop into a planet that close to a star. Instead, if a massive planet formed far from its star, it could move to a short orbit via disk-driven migration or high-eccentricity tidal migration (Dawson & Johnson 2018). If the hot Jupiter were primordially misaligned, this would indicate disk-driven migration, whereas post-formation misalignment could result from high-eccentricity tidal migration.

Constraints on which mechanisms actually contribute to spin-orbit misalignment can be placed using the observed distribution of obliquities and trends across system parameters. Additional constraints on primordial misalignment can be placed using observations of circumstellar disks and their stars. Watson et al. (2011) first compared stellar inclinations to disk inclinations for 8 systems with spatially resolved debris disks, while Greaves et al. (2014) later did the same for 10 systems imaged by the *Herschel* satellite. Neither found evidence for misalignment, but both had limited samples and predate many spatially resolved images of disks taken by the Atacama Large Millimeter/submillimeter Array (ALMA), Hubble Space Telescope (HST), and Gemini Planet Imager (GPI) that can robustly measure disk inclinations. Davies (2019) compared inclinations for resolved disks (mostly protoplanetary) in the  $\rho$  Ophiuchus and Upper Scorpius star forming regions, finding that a third of systems are potentially misaligned. Davies (2019) used these contrasting results to raise the additional question of whether or not debris disks preserve the preceding protoplanetary disks' geometry and if star-disk-planet interactions or the formation of a debris disk can change the star-disk obliquity.

In this work, we study the star-disk alignment for an expanded sample of 31 resolved debris disks. In Section 2, we outline our methods, including the sample selection and measurements made. We then discuss our results in Section 3. Finally, in Section 4, we conclude our findings.

## 2. METHODS

We assembled a list of spatially resolved debris disks from the literature, excluding circumbinary and circumtriple disks to simplify our analysis. We then identified systems with published stellar inclinations ( $i_s$ ) or the data necessary to measure the inclination available, leaving a sample of 31 targets that can be found in Table 1.

Effective temperatures ( $T_{\text{eff}}$ ), masses ( $M$ ), and radii ( $R$ ) were taken from the *TESS* Input Catalog (TIC; Stassun et al. 2018; Paegert et al. 2021) for most stars in our sample. Given the majority resolved debris disks are located around nearby, bright stars, the TIC adopted most of these parameters from large spectroscopic catalogs, avoiding the challenges of color-temperature relationships discussed in Stassun et al. (2018), particularly for the coolest stars ( $T_{\text{eff}} < 3800$  K). Parallaxes are known for all objects in our sample, providing precise measurements of radius in the TIC. 4 targets (AU Mic, Vega,  $\beta$  Leonis, and  $\beta$  Pictoris) that were either missing measurements or were reported without uncertainties were supplemented using values found elsewhere in the literature. The number of confirmed planets in each system was additionally determined by searching the NASA Exoplanet Archive Confirmed Planets Table (NASA Exoplanet Archive 2019). 8 out of the 31 systems have at least one confirmed planet.

To determine the projected rotational velocities ( $v \sin i$ ) of our sample, we adopted published values for each target. If multiple values were found, we adopted the measurement made using the highest-resolution spectrograph. Only 1 object ( $\beta$  Leonis) had a  $v \sin i$  reported without uncertainties; we assume 10% error bars on this measurement, typical for the uncertainties in our sample. 2 objects (GJ 581 and HD 23484) had upper limits on their projected rotational velocities and were treated as such in our analysis. We note that spectral line broadening from rotation is degenerate with turbulence in the stellar atmosphere and the  $v \sin i$  measurements in this work use a variety of modeling frameworks to account for macroturbulence, possibly introducing unknown systematics to our analysis.

Archival rotation periods were gathered for 26 objects in our sample. We also directly measured the rotation period for stars that displayed quasiperiodic variations in the Pre-Search Data Conditioned Simple Aperture Photometry (PDCSAP) light curves produced by the *TESS* Science Processing Operations Center (SPOC), which have been corrected for instrumental systematics (Stumpe et al. 2012; Smith et al. 2012; Stumpe et al. 2014). Each photometric time series was modeled using a Gaussian process (GP), which are commonly used to represent rotational modulation induced by active regions rotating in and out of view (Haywood et al. 2014; Rajpaul et al. 2015). We used the rotation kernel implemented in `celerite2` that combines two dampened simple harmonic oscillators with periods of  $P$  and  $P/2$  to capture the stochastic variability in a star's rotation signal (Foreman-Mackey et al. 2017; Foreman-Mackey 2018).

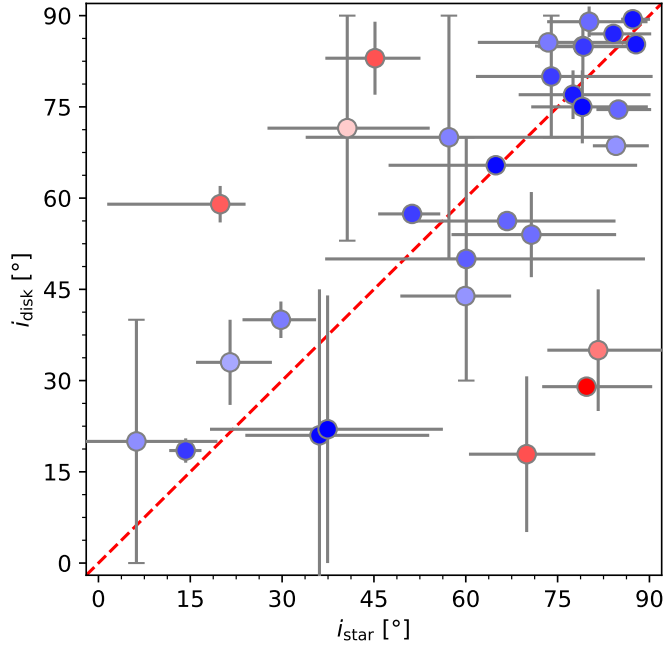


**Figure 1.** Disk inclinations plotted against the stellar inclinations for each system in our sample. The color of each point corresponds to the absolute value of the median of  $\Delta i = i_d - i_s$ , where blue indicates a well-aligned system and red indicates a large misalignment. Capped error bars represent the range of values that a parameter falls within (assuming a uniform distribution) while the rest represent the 68% credibility interval.

Using *TESS* data, we measured the rotation period of 18 stars, 5 of which had no previously published measurements; all of these measurements agree with either our archival values or the rotation period relationship in Noyes et al. (1984). For each of these 18 targets, we used the rotation periods and uncertainties determined using *TESS* data as they are well-constrained and measured under a standard framework. These periods, along with the projected rotational velocities and the corresponding uncertainties, can be found in Table 1 while the *TESS* light curves, GP models, and rotation period posteriors are shown in Appendix A.

We then determined the stellar inclination for each target with a known radius, rotation period, and  $v \sin i$  using the projected rotational velocity method, where the inclination is given by

$$i = \arcsin \left( \frac{v \sin i}{v} \right) = \arcsin \left( \frac{v \sin i}{2\pi R/P} \right). \quad (1)$$

As discussed by Masuda & Winn (2020),  $v \sin i$  and  $v$  are not independent from each other, complicating the statistical inference of  $i$ . A simple technique accounting for this is to use a Markov chain Monte Carlo (MCMC) process with a uniform prior on  $\cos i$  and measurement informed priors on  $R$ ,  $P$ , and  $(2\pi R/P)\sqrt{1 - \cos^2 i}$  (Albrecht et al. 2022). This approach is also advantageous because it easily accounts for uncertainties in our measurements of  $R$ ,  $P$ , and  $v \sin i$ . Given that measurements of  $v \sin i$  are typically made from a star's spectral absorption lines and require that broadening from rotation be distinguished from other sources, including turbulence in the stellar atmosphere or instrumental resolution, the projected rotational velocity method is often subject to systematic uncertainties. Therefore, we adopted stellar inclinations previously determined using more accurate methods such as interferometry (Vega and  $\beta$  Leonis), asteroseismology ( $\beta$  Pictoris), and starspot tracking ( $\epsilon$  Eridani) whenever possible. Interferometry and asteroseismology also allow us to expand our sample to early-type stars with weak, often undetectable rotational modulation.

We conducted a literature search for disk inclinations ( $i_d$ ), selecting values that were the most well-constrained, typically corresponding to images with the highest spatial resolution. Most of these images were taken using ALMA, HST, and GPI, although the uncertainties on the inclinations vary widely as the spatial resolution is highly dependent on instrument configuration and distance. Inclinations can also be determined more precisely for edge-on disks than face-on disks.

To better understand whether the star and disk might be misaligned, we calculated the difference between the disk and stellar inclinations ( $\Delta i = i_d - i_s$ ), the absolute value of which gives the minimum star-disk misalignment; because we are unable to determine the position angle of the stellar rotation axis or the direction of the disk and stellar angular momenta, we are unable to calculate the full obliquity. For systems with stellar inclinations determined using the projected rotational velocity technique, we assumed the MCMC posterior distribution; for the systems with archival measurements, a sample of stellar inclinations were drawn from Gaussian distributions. Similarly, we drew a sample of disk inclinations using either uniform or Gaussian distributions when appropriate. We then took the differences between our samples of disk and stellar inclinations and adopted the median value along with lower and upper uncertainties representative of the 68% credibility interval. These differences, along with the stellar and disk inclinations, are given in Table 2.

### 3. RESULTS AND DISCUSSION

#### 3.1. Comparing Disk and Stellar Inclinations

25 systems appear to be closely aligned with disk and stellar inclinations consistent of being within  $10^\circ$  of each other (although large uncertainties mean that some of these systems could still be misaligned). There are several exceptions; most notably, HD 10647, HD 138813, HD 191089, HD 30447,  $\epsilon$  Eridani, and  $\tau$  Ceti all have misalignments ranging roughly between  $30^\circ$  and  $60^\circ$ . If stars and their disks are well-aligned, we would expect to see a monotonic, increasing relationship between disk inclination and stellar inclination in Figure 1. We test how well-aligned systems tend to be by calculating the Spearman rank-order correlation coefficient ( $r_S$ ) for our data set. Using the median values for our inclinations, we find a coefficient of 0.62 with a p-value of 0.0002; however, this does not reflect the broad uncertainties on some of the inclination measurements. For each disk and stellar inclination, we drew a random sample and calculated a new coefficient and the corresponding p-value  $10^4$  times. The 68% credibility interval for  $r_S$  was  $.54 \pm 0.08$  with p-values of  $0.0008^{+0.0036}_{-0.00069}$ . These values for  $r_S$  are notably lower than the coefficient of 0.82 found by Watson et al. (2011) and indicate that while there is a positive correlation between disk and stellar inclinations, they are not always well-aligned.

It is important to keep in mind that disk and stellar inclinations can only put a lower limit on misalignment and that a full analysis requires knowledge of both the disk and stellar position angle on the sky plane. Further, inclinations do not indicate the directions that the star is rotating and the disk material is orbiting; if they are moving in opposite directions, the misalignment between the disk and star would be much greater than calculated. Given that systems such as K2-290—a strong candidate for primordial misalignment—have co-planar planets in retrograde orbits, this may be a significant bias (Hjorth et al. 2021).

While Watson et al. (2011) and Greaves et al. (2014) did not find signs of star-disk misalignment in their sample of debris disks, Davies (2019) observed misalignment of protoplanetary disks at a rate slightly higher than seen in our analysis ( $\sim 33\%$ ); however, we note that they observed much smaller misalignments, typically less than  $30^\circ$ . This indicates that the star-disk misalignment may not decrease as the disk transitions, as suggested by Davies (2019), and raises the question of whether misalignment increases as the system evolves. It is possible that mechanisms such as stellar flybys can incline debris disks (Moore et al. 2020) while processes such as accretion onto the star are unlikely to realign the system.

Figure 2 shows the mass, radius,  $v \sin i$ , and rotation period of each star in our sample versus the effective temperature. Figure 3 shows the difference between the disk and stellar inclinations as a function of system parameters. In these plots, we see most of the star-disk systems are well-aligned aside from the 6 mentioned above. The misaligned systems are not clustered around any specific  $T_{\text{eff}}$  or mass, suggesting that misalignment may occur regardless of stellar type, although there are not enough stars to make definitive conclusions. We also do not observe misalignment occurring more frequently with the presence of known planets; yet, many substellar objects in these debris disk systems may easily be undetectable. Finally, the 6 significantly misaligned systems span a wide range of ages ( $\sim 7$  Myr to 5.8 Gyr; Mamajek & Hillenbrand 2008; Bell et al. 2015; Pecaut & Mamajek 2016; Shkolnik et al. 2017; Nielsen et al. 2019); this is not surprising given that primordial misalignment is expected to occur during the protoplanetary disk stage, well before debris disks form.

#### 3.2. Implications for Primordial Misalignment

If magnetic warping were responsible for spin-orbit misalignment, Spalding & Batygin (2015) argue that misalignment should occur more frequently around stars with masses greater than  $1.2 M_\odot$ ; this is because lower-mass, young stars

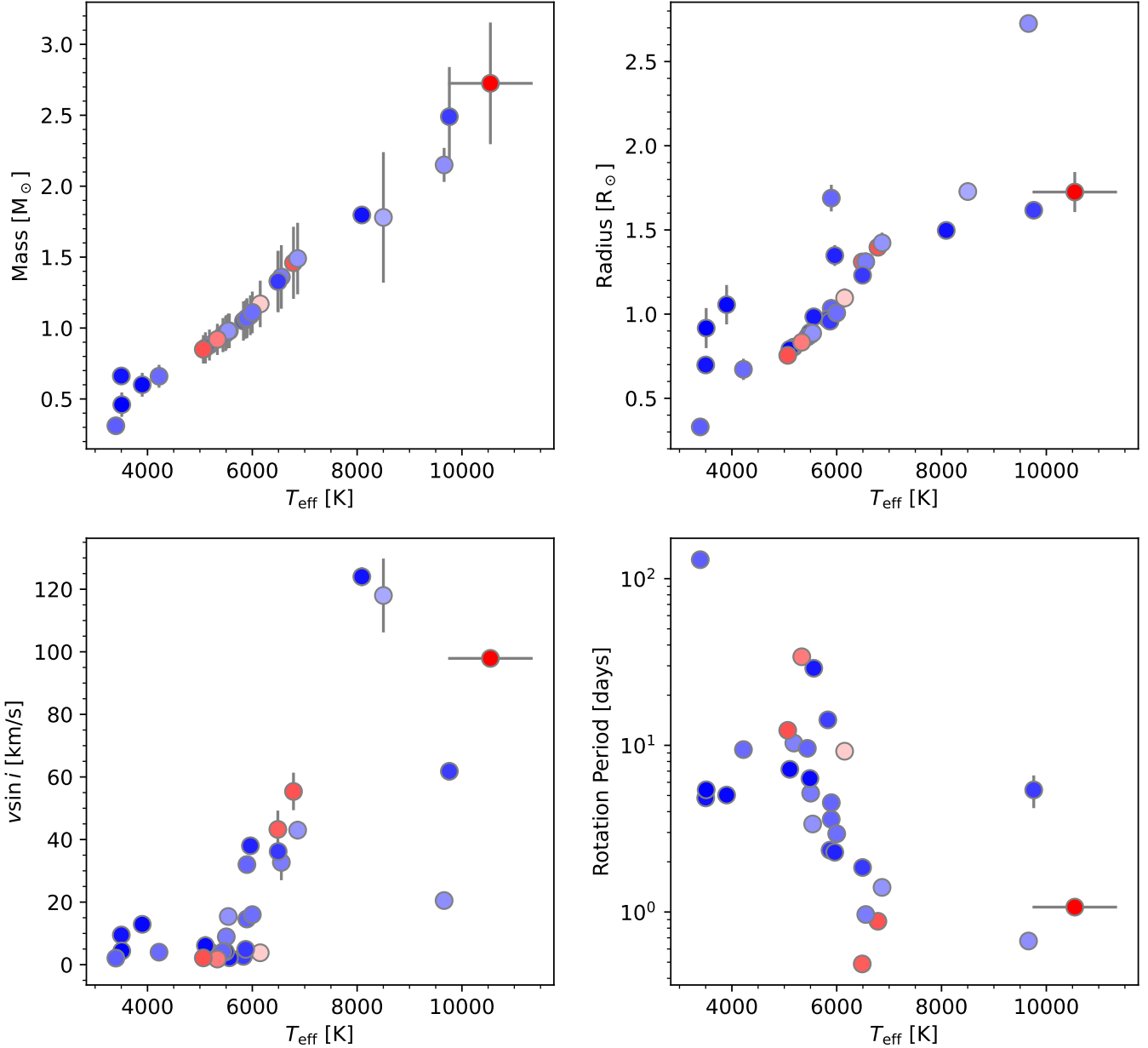


**Figure 2.** Stellar parameters for the systems in our sample. The color of each point corresponds to the absolute value of the median of  $\Delta i = i_d - i_s$ , where blue indicates a well-aligned system and red indicates a large misalignment. The top left figure shows mass versus  $T_{\text{eff}}$ , the top right shows radius versus  $T_{\text{eff}}$ , the bottom left gives  $v \sin i$  versus  $T_{\text{eff}}$ , and the bottom right gives the rotation period versus  $T_{\text{eff}}$ .

would be able to realign their stellar spin axes with the surrounding disks due to their stronger magnetic fields. As seen in Figure 3, 2 of the significantly misaligned systems ( $\epsilon$  Eridani and  $\tau$  Ceti) have stellar masses below  $1.2 M_{\odot}$  while 2 (HD 10647 and HD 191089) have masses very close to this limit, suggesting that magnetic warping alone is not a viable mechanism for disk misalignment.

If chaotic accretion were at play, subsequent accretion of disk material onto the star is expected to reduce the misalignment to values lower than  $20^\circ$  by the time planets begin to form (Takaishi et al. 2020). Not only does this fail to describe the distribution of obliquities observed for exoplanets, but it does not match the  $\sim 30^\circ - 60^\circ$  misalignments shown in Figure 3. We do see systems with small potential misalignments near or below  $20^\circ$ , including HD 107146, HD 129590, HD 145560, HD 202917, HD 206893, HD 35650, HD 377, and  $\beta$  Leonis, but the large uncertainties on our

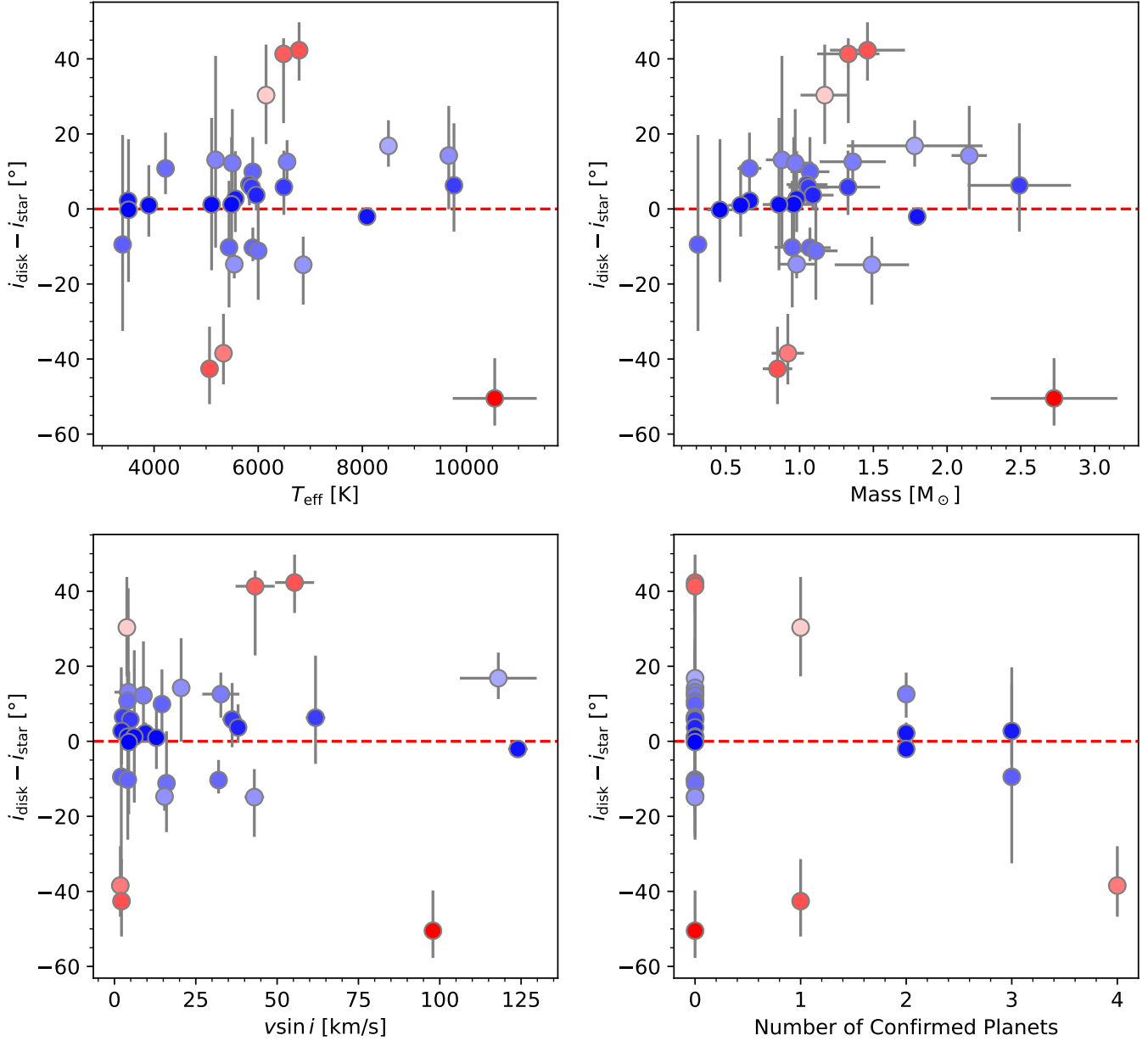


**Figure 3.** The difference between the disk and stellar inclinations ( $i_d - i_s$ ) plotted versus different system parameters. The color of each point corresponds to the median value of the minimum obliquity. The top left shows  $T_{\text{eff}}$  on the bottom axis while the right has the mass, the bottom left shows  $v \sin i$ , and the bottom right the number of confirmed planets in the system.

obliquity measurements make it difficult to determine whether low-obliquity systems are truly misaligned. Additionally, without knowing the position angles of each star, we cannot definitively comment on whether star-disk misalignment commonly falls near  $20^\circ$ .

While the significantly misaligned disks could have been torqued out of alignment by an inclined stellar or planetary companion, this mechanism is unable to explain the observed distribution of spin-orbit obliquities (Zanazzi & Lai 2018; Albrecht et al. 2022). Ultimately, it is unclear what mechanisms can misalign disks around their stars; further, because we do not know of many planets in these systems, we are unable to determine whether the same mechanisms could be responsible for spin-orbit misalignment. As discussed in Section 3.1, mechanisms such as stellar flybys may incline debris disks in addition to planetary orbits, and the obliquities measured in this work may not reflect a system's primordial architecture.

#### 4. CONCLUSIONS

We investigate the alignment of resolved debris disks with their stars, placing a lower limit on their obliquities by comparing stellar and disk inclinations. With recent resolved images of disks taken by ALMA, HST, and GPI, along with rotation periods measured using *TESS*, we were able to include 31 systems in our analysis, more than 3 times as large as the samples included in previous studies of debris disks.

While there formerly was little evidence for misalignment between debris disks and their stars, we find 6 systems with disk and stellar inclinations separated by  $\sim 30^\circ - 60^\circ$ . This indicates that these evolved disks are frequently misaligned with their stars; although, systems are more often well-aligned than not. Given that we observe such large minimum obliquities, some mechanism other than chaotic accretion needs to be at play. We also see misaligned systems with stellar masses below or near  $1.2 M_\odot$ , suggesting that magnetic warping alone cannot be responsible for misalignment. Because resonant processes that could torque the disk out of alignment fail to explain the distribution of spin-orbit obliquities, it remains unclear what role primordial misalignment could play in shaping planetary systems. Further, it is unknown whether these disk obliquities truly reflect the structure of the preceding protoplanetary disk.

Future work needs to expand the number of debris disk hosts with inclination measurements, helping constrain the characteristics of misaligned systems. Few stars in our sample have known planetary companions and no confirmed hot Jupiter systems are currently known to contain circumstellar debris; searching for dust in confirmed planetary systems could help better understand whether the mechanisms that misalign disks with their stars are also responsible for spin-orbit misalignment.

Existing methods to measure stellar position angle cannot be applied to the vast majority of debris disk hosts (Le Bouquin et al. 2009; Lesage & Wiedemann 2014), meaning the full obliquity between a disk and its star cannot be measured. As mentioned by Watson et al. (2011), a full Bayesian analysis accounting for this limitation could place more useful upper limits on the misalignment, similar to the framework presented in Fabrycky & Winn (2009) for spin-orbit angles. Regardless, the lower limits on misalignment presented in this work help better understand the geometry of debris disks, and future observations will improve our understanding of the mechanisms that shape and misalign these systems.

We thank the referee for thorough and insightful feedback that greatly improved the quality of this paper. We also thank Ruth Angus and Megan Bedell for a helpful discussion on how to measure stellar rotation periods and Ann-Marie Madigan and Carolyn Crow for thoughtful conversation about our results. M.A.M. acknowledges support for this work from the National Aeronautics and Space Administration (NASA) under award number 19-ICAR19\_2-0041. This research has made use of the NASA Exoplanet Archive, which is operated by the California Institute of Technology, under contract with the National Aeronautics and Space Administration under the Exoplanet Exploration Program. This work made use of the SIMBAD database (operated at CDS, Strasbourg, France), NASA's Astrophysics Data System Bibliographic Services. The TIC data presented in this paper were obtained from the Mikulski Archive for Space Telescopes (MAST) at the Space Telescope Science Institute and can be accessed via [10.17909/fwdt-2x66](https://doi.org/10.17909/fwdt-2x66). This research has made use of the VizieR catalog access tool, CDS, Strasbourg, France (DOI: 10.26093/cds/vizier). The original description of the VizieR service was published in A&AS 143, 23. This work has made use of data from the European Space Agency (ESA) mission *Gaia* (<https://www.cosmos.esa.int/gaia>), processed by the *Gaia* Data Processing and Analysis Consortium (DPAC, <https://www.cosmos.esa.int/web/gaia/dpac/consortium>). Funding for the DPAC has been provided by national institutions, in particular the institutions participating in the *Gaia* Multilateral Agreement.

*Software:* `astropy` (Astropy Collaboration et al. 2018), `exoplanet` (Foreman-Mackey et al. 2021), `matplotlib` (Hunter 2007), `numpy` (Harris et al. 2020), `PyMC3` (Salvatier et al. 2016), `SciPy` (Virtanen et al. 2020)

Table 1. Sample of Disk Hosts and Stellar Properties

Name	Spt	$T_{\text{eff}}$ (K)	Mass ( $M_{\odot}$ )	Radius ( $R_{\odot}$ )	$v \sin i$ ( $\text{km s}^{-1}$ )	$P_{\text{rot}}$ (days)	$N_{\text{planets}}$	SpT	$T_{\text{eff}}$	Mass	Radius	$v \sin i$	$P_{\text{rot}}$	References
61 Virginis	G6.5V	5562 ± 110	0.98 ± 0.12	0.984 ± 0.045	2.2 ± 0.3	29.0	3 <sup>a</sup>	1	2	2	2	3	4	
AU Mic	M1VeBaI	3500 ± 100	0.66 ± 0.02	0.698 ± 0.021	9.5 ± 0.2	4.8366 ± 0.0075	2 <sup>b</sup>	1	5	2	2	6	7	
GJ 581	M3V	3396 ± 160	0.31 ± 0.02	0.33 ± 0.01	≤ 2.1	130 ± 2	3 <sup>c</sup>	8	2	2	2	9	10	
HD 104860	G0/F9V	6000 ± 150	1.11 ± 0.15	1.007 ± 0.054	16 ± 2	2.9493 ± 0.0031	0	11	2	2	2	11	7	
HD 10647	F9V	6151 ± 150	1.17 ± 0.16	1.096 ± 0.057	3.8 ± 0.4	9.22 ± 0.06	1 <sup>d</sup>	1	2	2	2	12	7	
HD 107146	G2V	5873 ± 110	1.06 ± 0.14	0.958 ± 0.041	4.9 ± 0.6	2.35	0	13	2	2	2	14	15	
HD 129590	G3V	5897 ± 130	1.07 ± 0.14	1.689 ± 0.079	32 ± 2	4.5291 ± 0.0061	0	16	2	2	2	17	7	
HD 138813	A0V	10543 ± 810	2.72 ± 0.43	1.72 ± 0.12	97.9 ± 2.2	1.07	0	18	2	2	2	19	20	
HD 141943	G2	5963 ± 120	1.09 ± 0.14	1.348 ± 0.062	38 ± 2	2.283 ± 0.062	0	21	2	2	2	22	7	
HD 145560	F5V	6865 ± 140	1.49 ± 0.25	1.423 ± 0.061	43 ± 3	1.40473 ± 0.00061	0	23	2	2	2	17	7	
HD 166	G8	5489 ± 140	0.96 ± 0.12	0.89 ± 0.052	4.1 ± 0.4	6.3265 ± 0.0082	0	24	2	2	2	25	7	
HD 181296	A0V	9760 ± 140	2.49 ± 0.35	1.617 ± 0.042	62 ± 3	5.4 ± 1.2	0	26	2	2	2	27	27	
HD 191089	F5V	6487 ± 110	1.33 ± 0.21	1.31 ± 0.053	43 ± 6	0.488 ± 0.005	0	16	2	2	2	27	7	
HD 202628	G5V	5831 ± 130	1.05 ± 0.14	0.97 ± 0.05	2.65 ± 0.11	14.215 ± 0.091	0	21	2	2	2	29	7	
HD 202917	G7V	5541 ± 140	0.98 ± 0.12	0.887 ± 0.052	15.4 ± 0.1	3.3739 ± 0.0036	0	21	2	2	2	21	7	
HD 206893	F5V	6554 ± 120	1.36 ± 0.22	1.311 ± 0.055	32.7 ± 5.7	0.966 ± 0.003	2 <sup>e</sup>	30	2	2	2	31	32	
HD 23484	K2V	5182 ± 140	0.88 ± 0.11	0.804 ± 0.054	≤ 4.2	10.32 ± 0.83	0	21	2	2	2	21	7	
HD 30447	F3V	6786 ± 110	1.46 ± 0.25	1.397 ± 0.053	55 ± 6	0.88 ± 0.02	0	16	2	2	2	27	27	
HD 35650	K6V	4220 ± 130	0.66 ± 0.081	0.672 ± 0.063	4.0 ± 0.2	9.43 ± 0.03	0	21	2	2	2	21	7	
HD 35841	F3V	6493 ± 130	1.33 ± 0.22	1.231 ± 0.051	36 ± 3	1.849 ± 0.019	0	18	2	2	2	27	7	
HD 377	G2V	5895 ± 140	1.07 ± 0.13	1.034 ± 0.055	14.6 ± 0.5	3.601 ± 0.046	0	21	2	2	2	25	7	
HD 53143	G9V	5440 ± 100	0.95 ± 0.12	0.864 ± 0.039	4 ± 1	9.592 ± 0.027	0	21	2	2	2	33	7	
HD 61005	G8V <sub>k</sub>	5503 ± 110	0.97 ± 0.12	0.878 ± 0.039	8.9 ± 1.5	5.1639 ± 0.0078	0	30	2	2	2	27	7	
HD 92945	K1V	5105 ± 150	0.86 ± 0.11	0.791 ± 0.056	6 ± 3	7.18 ± 0.31	0	21	2	2	2	34	7	
TWA 25	M0.5	3899 ± 120	0.6 ± 0.084	1.06 ± 0.12	12.9 ± 1.2	5.0318 ± 0.0079	0	35	2	2	2	36	7	
TWA 7	M2Ve	3509 ± 120	0.46 ± 0.086	0.92 ± 0.12	4.4 ± 1.2	5.41 ± 0.37	0	21	2	2	2	21	7	
Vega	A0Va	9660 ± 90	2.15 ± 0.12	2.726 ± 0.006	20.5 ± 0.7	0.67 ± 0.07	0	37	38	38	38	39	40	

Table 1 continued on next page

**Table 1** (*continued*)

Name	Spt	$T_{\text{eff}}$ (K)	Mass ( $M_{\odot}$ )	Radius ( $R_{\odot}$ )	$v \sin i$ ( $\text{km s}^{-1}$ )	$P_{\text{rot}}$ (days)	$N_{\text{planets}}$	SpT	$T_{\text{eff}}$	Mass	Radius	$v \sin i$	$P_{\text{rot}}$	References
$\beta$ Leonis	A3Va	8502 ± 45	1.93 ± 0.01	2.28 ± 0.11	118 ± 12	...	0	41	2	42	43	43	...	
$\beta$ Pictoris	A6V	8143 ± 67	1.8 ± 0.04	1.54 ± 0.04	124 ± 3	...	2 <sup>f</sup>	30	44	44	45	45	...	
$\epsilon$ Eridani	K2V	5065 ± 100	0.9 ± 0.1	0.755 ± 0.038	2.17 ± 0.25	12.3 ± 0.06	1 <sup>g</sup>	1	2	2	2	6	46	
$\tau$ Ceti	G8V	5333 ± 99	0.92 ± 0.11	0.833 ± 0.037	1.8 ± 0.1	34.0	4 <sup>h</sup>	1	2	2	2	3	47	

<sup>a</sup>Planets around 61 Virginis detected via radial velocities and inclinations are unknown (Vogt et al. 2010).

<sup>b</sup>Planets follow edge-on orbits around AU Mic and are well-aligned with star and disk (Plavchan et al. 2020; Addison et al. 2021; Martioli et al. 2021).

<sup>c</sup>Planets around GJ 581 detected via radial velocities and inclinations are unknown (Trifonov et al. 2018).

<sup>d</sup>Planet around HD 10647 detected via radial velocities and inclination is unknown (Marmier et al. 2013).

<sup>e</sup>The two planets around HD 206893 have a mutual inclination of 15° at most and could be misaligned from the disk by ∼20° (Hinkley et al. 2022).

<sup>f</sup>Planets around  $\beta$  Pictoris detected via direct imaging and appear well-aligned with the disk (Feng et al. 2022).

<sup>g</sup>Orbital inclination of planet around  $\epsilon$  Eridani has large uncertainties, may be misaligned with the disk (Llop-Sayson et al. 2021; Benedict 2022).

<sup>h</sup>Planets around  $\tau$  Ceti detected via radial velocities and inclinations are unknown (Feng et al. 2017).

**References**—(1) Keenan & McNeil (1989), (2) 2021arXiv210804778P, (3) Reiners & Schmitt (2003), (4) Balinbas et al. (1996), (5) Plavchan et al. (2009), (6) Hojjatpanah et al. (2019), (7) This Work, (8) Stephenson (1986), (9) Glebocki & Gnatcinski (2005), (10) Robertson et al. (2014), (11) Kahraman Aligavus et al. (2016), (12) Soto & Jenkins (2018), (13) Harlan & Taylor (1970), (14) Brewer et al. (2016), (15) Rimoldini et al. (2012), (16) Houk (1982), (17) Chen et al. (2011), (18) Houk & Smith-Moore (1988), (19) Dahm et al. (2012), (20) Oelkers et al. (2018), (21) Torres et al. (2006), (22) Cutispoto et al. (2002), (23) Houk (1978), (24) Bidelman (1985), (25) Marsden et al. (2014), (26) Houk & Cowley (1975), (27) Zúñiga-Fernández et al. (2021), (28) Desidera et al. (2015), (29) dos Santos et al. (2016), (30) Gray et al. (2006), (31) Zakhozhay et al. (2022), (32) Delorme et al. (2017), (33) Saar & Osten (1997), (34) Strassmeier et al. (2000), (35) Herczeg & Hillenbrand (2014), (36) Malo et al. (2014), (37) Gray et al. (2003), (38) Monnier et al. (2012), (39) Saffe et al. (2021), (40) Hurt et al. (2021), (41) van Belle & von Braun (2009), (42) Di Folco et al. (2004), (43) Akeson et al. (2009), (44) Zwintz et al. (2019), (45) Koen et al. (2003), (46) Giguere et al. (2016), (47) Isaacson & Fischer (2010)

**Table 2.** Disk and Stellar Inclinations

Name	$i_{\text{disk}}$	Disk Imaging Facility	$i_{\star}$	Stellar Inclination Method	$\Delta i$	References	
						$i_{\text{disk}}$	$i_{\star}$
	(°)		(°)			(°)	
61 Virginis	77 ± 4	HSO	77.5 <sup>+8.7</sup> <sub>-13.0</sub>	$v \sin i$	2.7 <sup>+13.0</sup> <sub>-8.9</sub>	1	2
AU Mic	89.4 ± 0.1	GPI	87.3 <sup>+1.9</sup> <sub>-2.8</sub>	$v \sin i$	2.2 <sup>+2.8</sup> <sub>-1.9</sub>	3	2
GJ 581	[30.0,70.0]	HSO	60.0 <sup>+21.0</sup> <sub>-28.0</sub>	$v \sin i$	-9.0 <sup>+29.0</sup> <sub>-23.0</sub>	4	2
HD 104860	54 ± 7	HSO	71.0 ± 13.0	$v \sin i$	-11.0 <sup>+14.0</sup> <sub>-13.0</sub>	5	2
HD 10647	[53.0,90.0]	HSO	40.6 <sup>+6.4</sup> <sub>-5.6</sub>	$v \sin i$	30.0 <sup>+14.0</sup> <sub>-13.0</sub>	6	2
HD 107146	18 ± 2	HST	14.2 <sup>+2.4</sup> <sub>-2.3</sub>	$v \sin i$	5.8 <sup>+2.6</sup> <sub>-2.7</sub>	7	2
HD 129590	74.56 ± 0.05	SPHERE/VLT	84.9 <sup>+3.6</sup> <sub>-5.4</sub>	$v \sin i$	-10.3 <sup>+5.4</sup> <sub>-3.6</sub>	8	2
HD 138813	29.0 ± 0.3	ALMA	79.7 <sup>+7.3</sup> <sub>-11.0</sub>	$v \sin i$	-50.5 <sup>+11.0</sup> <sub>-7.3</sub>	9	2
HD 141943	87 ± 1	GPI	84.1 <sup>+4.1</sup> <sub>-6.2</sub>	$v \sin i$	3.7 <sup>+6.2</sup> <sub>-4.1</sub>	3	2
HD 145560	43.9 ± 1.5	GPI	59.9 <sup>+11.0</sup> <sub>-7.5</sub>	$v \sin i$	-14.9 <sup>+7.5</sup> <sub>-11.0</sub>	10	2
HD 166	21 ± 24	HSO	36.1 <sup>+5.4</sup> <sub>-4.5</sub>	$v \sin i$	1.0 <sup>+18.0</sup> <sub>-12.0</sub>	5	2
HD 181296	[70.0,90.0]	Gemini South	74.0 <sup>+11.0</sup> <sub>-16.0</sub>	$v \sin i$	6.0 <sup>+17.0</sup> <sub>-12.0</sub>	11	2
HD 191089	59 ± 3	HST	19.9 <sup>+20.0</sup> <sub>-3.6</sub>	$v \sin i$	41.3 <sup>+4.2</sup> <sub>-19.0</sub>	12	2
HD 202628	57.4 ± 0.4	ALMA	51.2 <sup>+5.5</sup> <sub>-4.6</sub>	$v \sin i$	6.5 <sup>+4.6</sup> <sub>-5.6</sub>	13	2
HD 202917	68.6 ± 1.5	HST	84.5 <sup>+3.8</sup> <sub>-5.4</sub>	$v \sin i$	-14.7 <sup>+5.4</sup> <sub>-3.8</sub>	14	2
HD 206893	40 ± 3	ALMA	29.8 <sup>+6.0</sup> <sub>-5.6</sub>	$v \sin i$	12.6 <sup>+5.8</sup> <sub>-6.3</sub>	15	2
HD 23484	[50.0,90.0]	Herschel	57.0 <sup>+22.0</sup> <sub>-26.0</sub>	$v \sin i$	13.0 <sup>+28.0</sup> <sub>-23.0</sub>	16	2
HD 30447	83 ± 6	GPI	45.2 <sup>+7.6</sup> <sub>-6.2</sub>	$v \sin i$	42.3 <sup>+7.5</sup> <sub>-8.1</sub>	3	2
HD 35650	89.0 ± 2.5	HST	80.1 <sup>+6.9</sup> <sub>-9.4</sub>	$v \sin i$	10.8 <sup>+9.6</sup> <sub>-6.9</sub>	17	2
HD 35841	84.9 ± 0.2	GPI	79.2 <sup>+7.4</sup> <sub>-9.7</sub>	$v \sin i$	5.8 <sup>+9.7</sup> <sub>-7.4</sub>	18	2
HD 377	85 <sup>a</sup>	HST	79.1 <sup>+7.4</sup> <sub>-8.9</sub>	$v \sin i$	9.9 <sup>+9.3</sup> <sub>-7.8</sub>	17	2
HD 53143	56.23 ± 0.37	ALMA	67.0 <sup>+16.0</sup> <sub>-18.0</sub>	$v \sin i$	-10.0 <sup>+18.0</sup> <sub>-16.0</sub>	19	2
HD 61005	85.6 ± 0.1	ALMA	73.0 <sup>+12.0</sup> <sub>-14.0</sub>	$v \sin i$	12.0 <sup>+14.0</sup> <sub>-12.0</sub>	20	2
HD 92945	65.4 ± 0.9	ALMA	65.0 <sup>+18.0</sup> <sub>-23.0</sub>	$v \sin i$	1.0 <sup>+23.0</sup> <sub>-18.0</sub>	21	2
TWA 25	75 ± 6	HST	79.0 <sup>+7.6</sup> <sub>-10.0</sub>	$v \sin i$	1.0 <sup>+11.0</sup> <sub>-8.4</sub>	17	2
TWA 7	22 ± 22	HST	37.0 <sup>+17.0</sup> <sub>-11.0</sub>	$v \sin i$	0.0 ± 19.0	17	2
Vega	[0.0,40.0]	ALMA	6.2 ± 0.4	Interferometry	14.0 <sup>+13.0</sup> <sub>-14.0</sub>	22	23
$\beta$ Leonis	33 ± 7	HSO	21.5 ± 5.0	Interferometry	16.8 <sup>+6.9</sup> <sub>-5.6</sub>	24	25
$\beta$ Pictoris	85.3 ± 0.3	GPI	87.8 ± 1.6	Asteroseismology	-2.0 <sup>+1.6</sup> <sub>-1.5</sub>	3	26
$\epsilon$ Eridani	18 ± 13	SMA/ATCA	69.95 <sup>+5.6</sup> <sub>-7.6</sub>	Photometry + Spectroscopy	-42.6 <sup>+11.0</sup> <sub>-9.5</sub>	27	28
$\tau$ Ceti	35 ± 10	HSO	81.6 <sup>+5.9</sup> <sub>-8.6</sub>	$v \sin i$	-38.4 <sup>+11.0</sup> <sub>-8.3</sub>	29	2

<sup>a</sup>No uncertainties reported. Standard deviation of 5° assumed.

**References**—(1) Wyatt et al. (2012), (2) This Work, (3) Esposito et al. (2020), (4) Lestrade et al. (2012), (5) Morales et al. (2016), (6) Liseau et al. (2010), (7) Schneider et al. (2014), (8) Matthews et al. (2017), (9) Hales et al. (2019), (10) Hom et al. (2020), (11) Smith et al. (2009), (12) Ren et al. (2019), (13) Faramaz et al. (2019), (14) Schneider et al. (2016), (15) Marino et al. (2020), (16) Ertel et al. (2014), (17) Choquet et al. (2016), (18) Esposito et al. (2018), (19) MacGregor et al. (2022), (20) MacGregor et al. (2018), (21) Marino et al. (2019), (22) Matrà et al. (2020), (23) Monnier et al. (2012), (24) Churcher et al. (2011), (25) Akeson et al. (2009), (26) Zwintz et al. (2019), (27) MacGregor et al. (2015), (28) Giguere et al. (2016), (29) Lawler et al. (2014)

## APPENDIX

A. *TESS* LIGHT CURVES AND MEASURED ROTATION PERIODS

A description of the light curve modeling approach is given in Section 2 while the derived rotation periods and  $1\sigma$  uncertainties are found in Table 1. We additionally calculate Lomb-Scargle periodograms for each light curve and the false alarm probability (FAP) associated with the rotation signal (Zechmeister & Kürster 2009). Several stars display double dipping, where two opposing star spots create a false signal at  $P/2$  (Basri & Nguyen 2018); in several instances, including HD 377 and HD 92945, we find that phase dispersion minimization periodograms (Stellingwerf 1978) better capture the true rotation period and use them in place of Lomb-Scargle periodograms. Figures 4 through 21 show a periodogram, phase-folded light curve, light curve from a single *TESS* sector, and the rotation period posterior for each object showing quasiperiodic variations in *TESS* data.

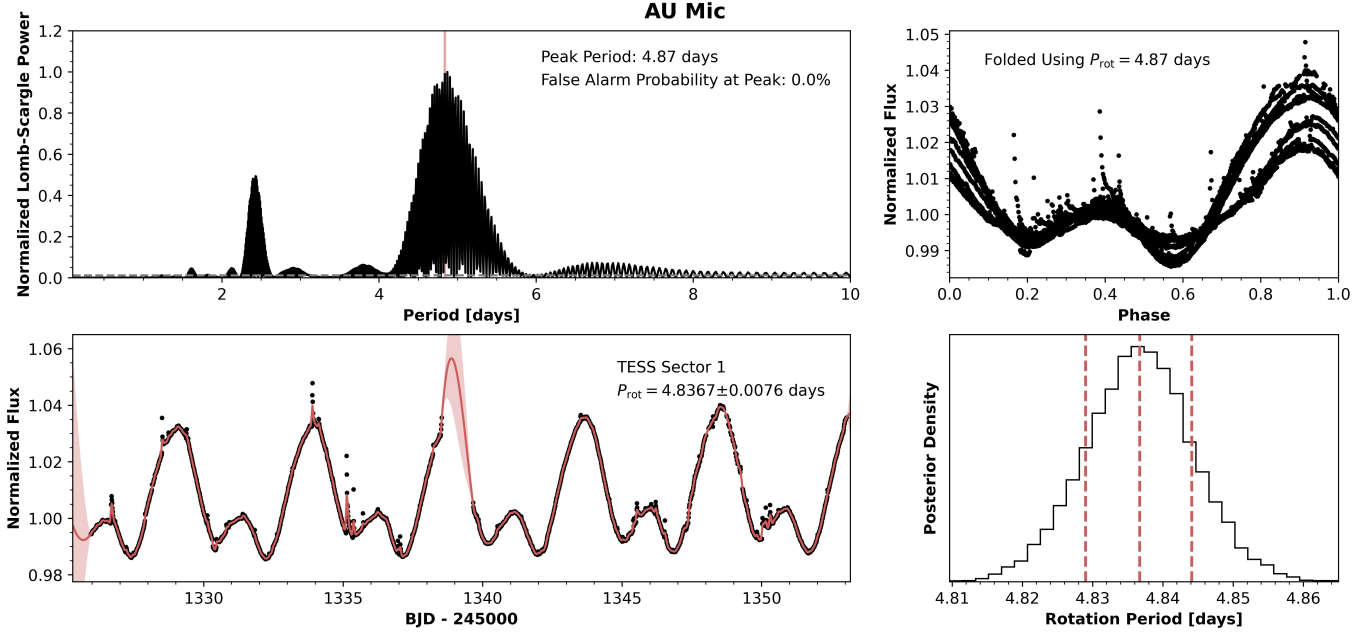


**Figure 4.** *Top left:* The Lomb-Scargle periodogram for the AU Mic *TESS* PDCSAP light curve is shown in black. The dashed grey line marks the 1% FAP level while the shaded red region denotes the  $1\sigma$  confidence interval for the rotation period posterior. *Top right:* The phase-folded light curve using the peak period from the Lomb-Scargle periodogram. *Bottom left:* The black points show data from *TESS* Sector 1 while the red line and shaded region mark the mean and  $1\sigma$  confidence interval for the GP model. *Bottom right:* The histogram shows the rotation period posterior derived from the GP model while the dash red lines mark the median and  $1\sigma$  interval.

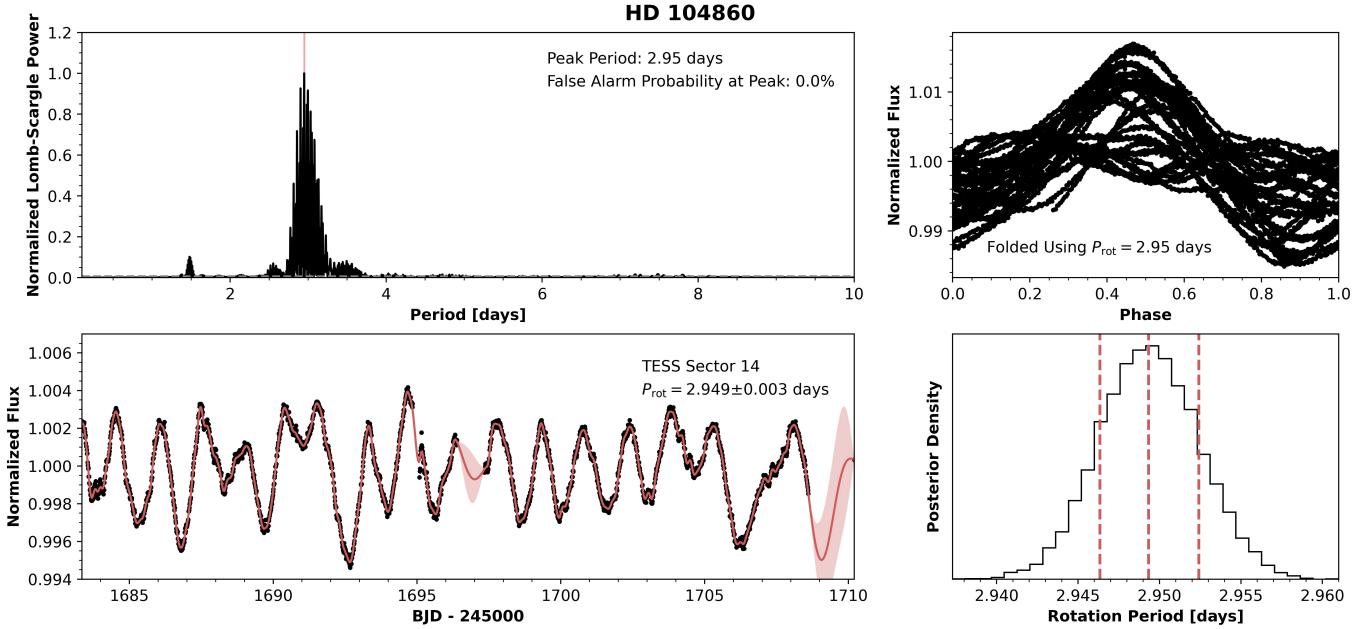


**Figure 5.** *Top left:* The Lomb-Scargle periodogram for the HD 104860 *TESS* PDCSAP light curve is shown in black. The dashed grey line marks the 1% FAP level while the shaded red region denotes the  $1\sigma$  confidence interval for the rotation period posterior. *Top right:* The phase-folded light curve using the peak period from the Lomb-Scargle periodogram. *Bottom left:* The black points show data from *TESS* Sector 14 while the red line and shaded region mark the mean and  $1\sigma$  confidence interval for the GP model. *Bottom right:* The histogram shows the rotation period posterior derived from the GP model while the dash red lines mark the median and  $1\sigma$  interval.

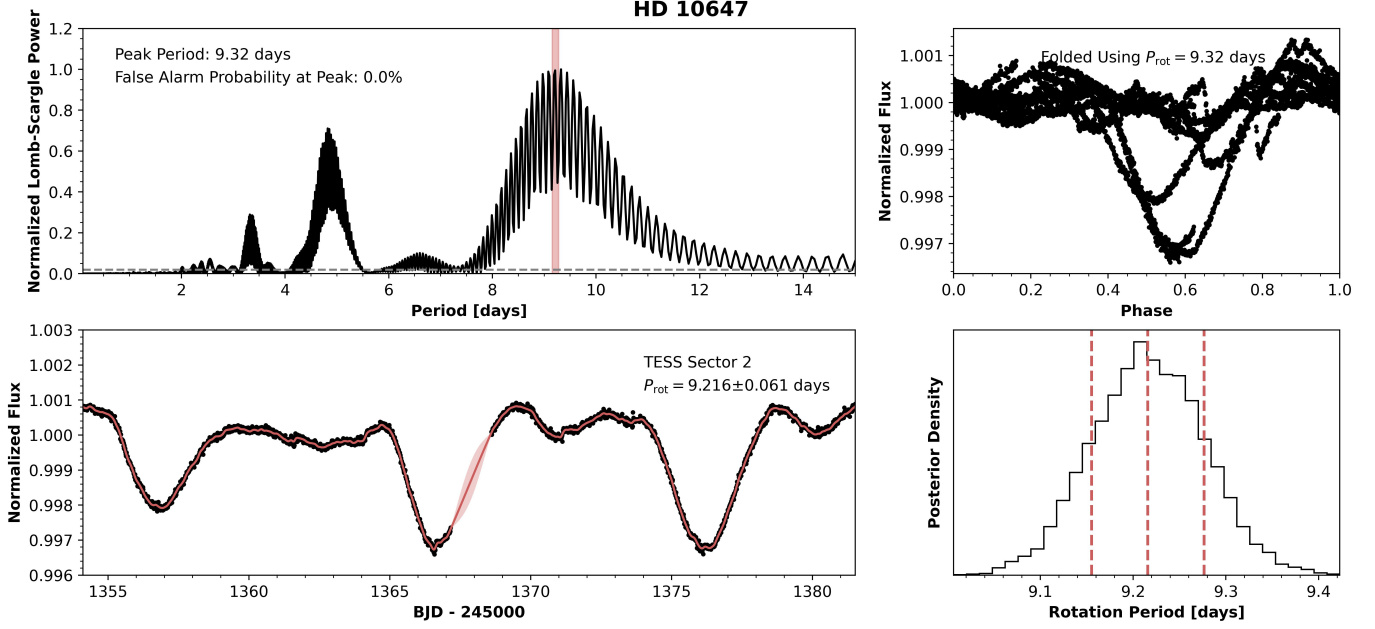


**Figure 6.** *Top left:* The Lomb-Scargle periodogram for the HD 10647 *TESS* PDCSAP light curve is shown in black. The dashed grey line marks the 1% FAP level while the shaded red region denotes the 1 $\sigma$  confidence interval for the rotation period posterior. *Top right:* The phase-folded light curve using the peak period from the Lomb-Scargle periodogram. *Bottom left:* The black points show data from *TESS* Sector 2 while the red line and shaded region mark the mean and 1 $\sigma$  confidence interval for the GP model. *Bottom right:* The histogram shows the rotation period posterior derived from the GP model while the dash red lines mark the median and 1 $\sigma$  interval.

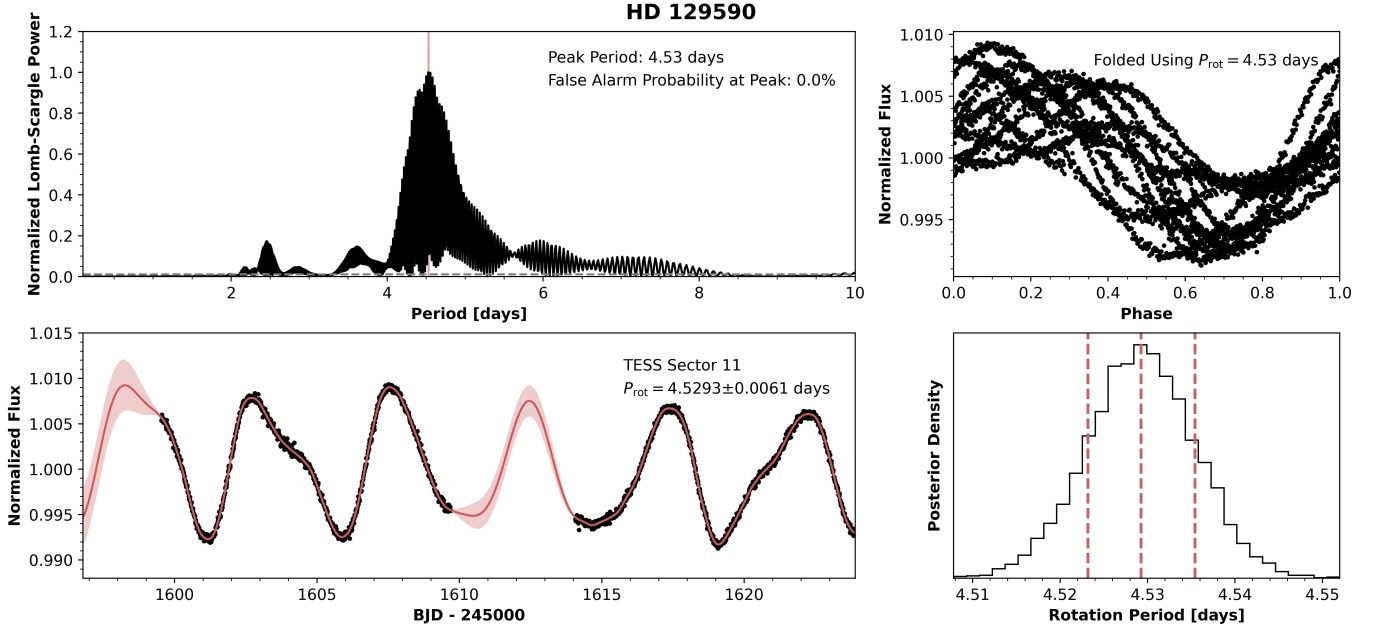


**Figure 7.** *Top left:* The Lomb-Scargle periodogram for the HD 129590 *TESS* PDCSAP light curve is shown in black. The dashed grey line marks the 1% FAP level while the shaded red region denotes the 1 $\sigma$  confidence interval for the rotation period posterior. *Top right:* The phase-folded light curve using the peak period from the Lomb-Scargle periodogram. *Bottom left:* The black points show data from *TESS* Sector 11 while the red line and shaded region mark the mean and 1 $\sigma$  confidence interval for the GP model. *Bottom right:* The histogram shows the rotation period posterior derived from the GP model while the dash red lines mark the median and 1 $\sigma$  interval.

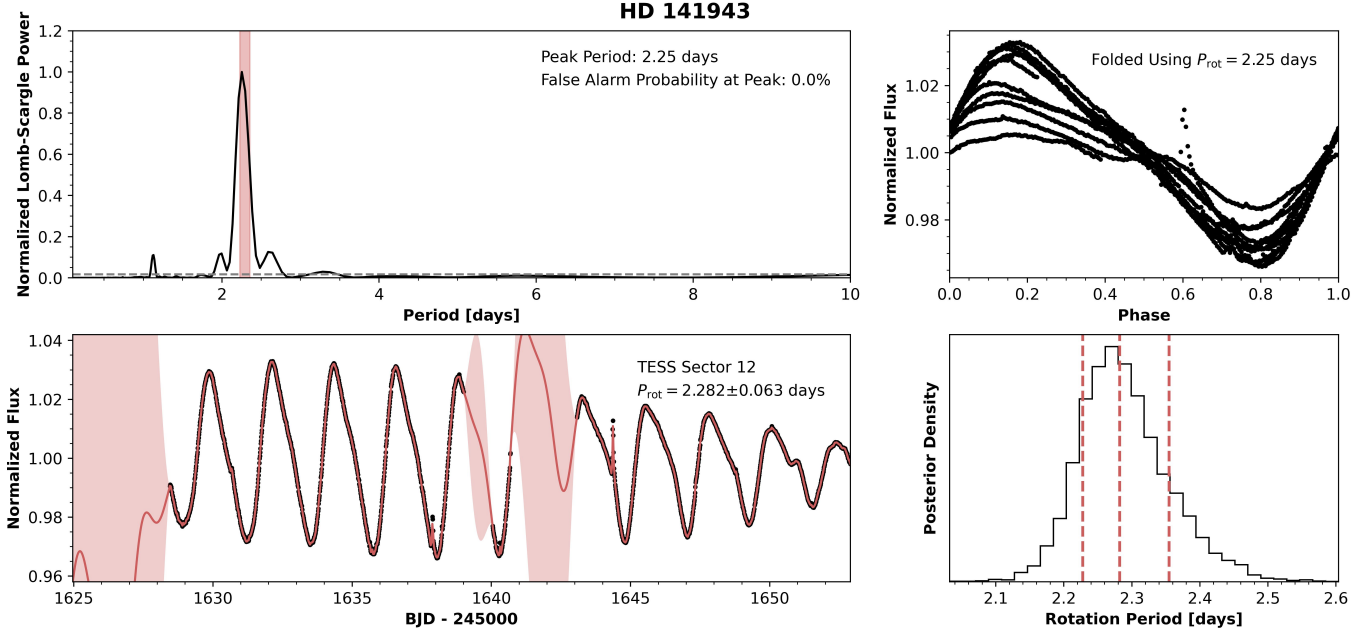


**Figure 8.** *Top left:* The Lomb-Scargle periodogram for the HD 141943 *TESS* PDCSAP light curve is shown in black. The dashed grey line marks the 1% FAP level while the shaded red region denotes the 1 $\sigma$  confidence interval for the rotation period posterior. *Top right:* The phase-folded light curve using the peak period from the Lomb-Scargle periodogram. *Bottom left:* The black points show data from *TESS* Sector 12 while the red line and shaded region mark the mean and 1 $\sigma$  confidence interval for the GP model. *Bottom right:* The histogram shows the rotation period posterior derived from the GP model while the dash red lines mark the median and 1 $\sigma$  interval.

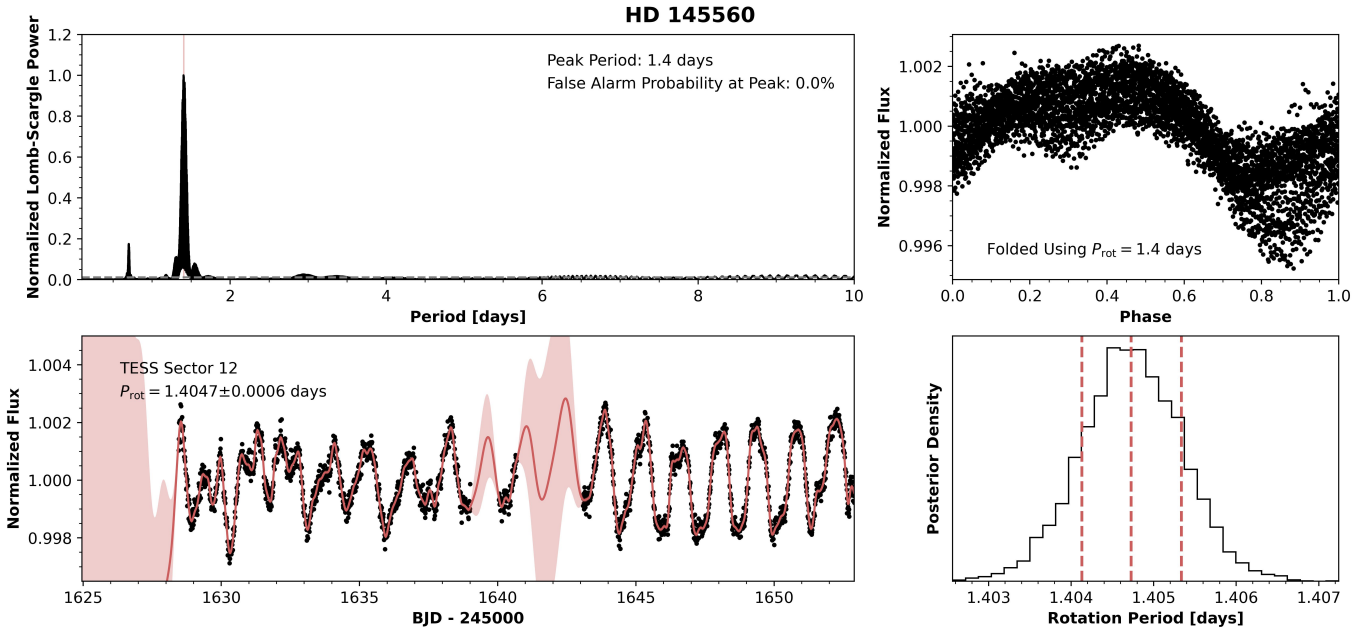


**Figure 9.** *Top left:* The Lomb-Scargle periodogram for the HD 145560 *TESS* PDCSAP light curve is shown in black. The dashed grey line marks the 1% FAP level while the shaded red region denotes the 1 $\sigma$  confidence interval for the rotation period posterior. *Top right:* The phase-folded light curve using the peak period from the Lomb-Scargle periodogram. *Bottom left:* The black points show data from *TESS* Sector 12 while the red line and shaded region mark the mean and 1 $\sigma$  confidence interval for the GP model. *Bottom right:* The histogram shows the rotation period posterior derived from the GP model while the dash red lines mark the median and 1 $\sigma$  interval.

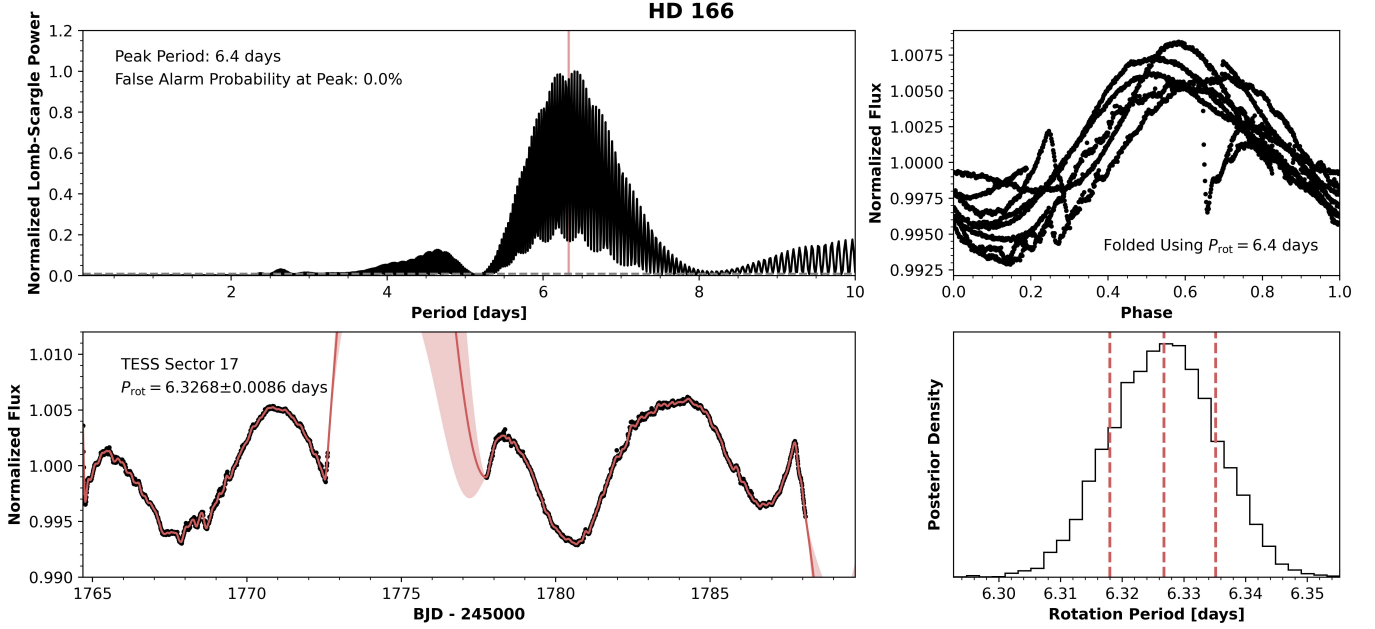


**Figure 10.** *Top left:* The Lomb-Scargle periodogram for the HD 166 *TESS* PDCSAP light curve is shown in black. The dashed grey line marks the 1% FAP level while the shaded red region denotes the  $1\sigma$  confidence interval for the rotation period posterior. *Top right:* The phase-folded light curve using the peak period from the Lomb-Scargle periodogram. *Bottom left:* The black points show data from *TESS* Sector 17 while the red line and shaded region mark the mean and  $1\sigma$  confidence interval for the GP model. *Bottom right:* The histogram shows the rotation period posterior derived from the GP model while the dash red lines mark the median and  $1\sigma$  interval.

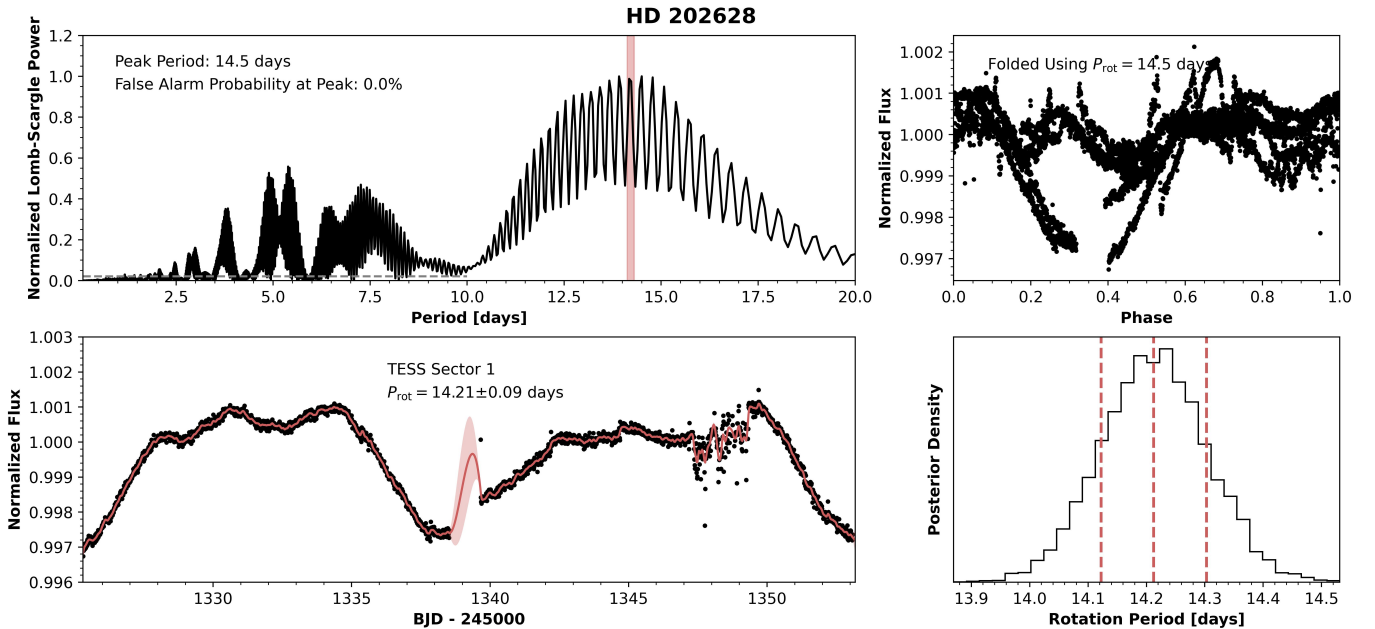


**Figure 11.** *Top left:* The Lomb-Scargle periodogram for the HD 202628 *TESS* PDCSAP light curve is shown in black. The dashed grey line marks the 1% FAP level while the shaded red region denotes the  $1\sigma$  confidence interval for the rotation period posterior. *Top right:* The phase-folded light curve using the peak period from the Lomb-Scargle periodogram. *Bottom left:* The black points show data from *TESS* Sector 1 while the red line and shaded region mark the mean and  $1\sigma$  confidence interval for the GP model. *Bottom right:* The histogram shows the rotation period posterior derived from the GP model while the dash red lines mark the median and  $1\sigma$  interval.

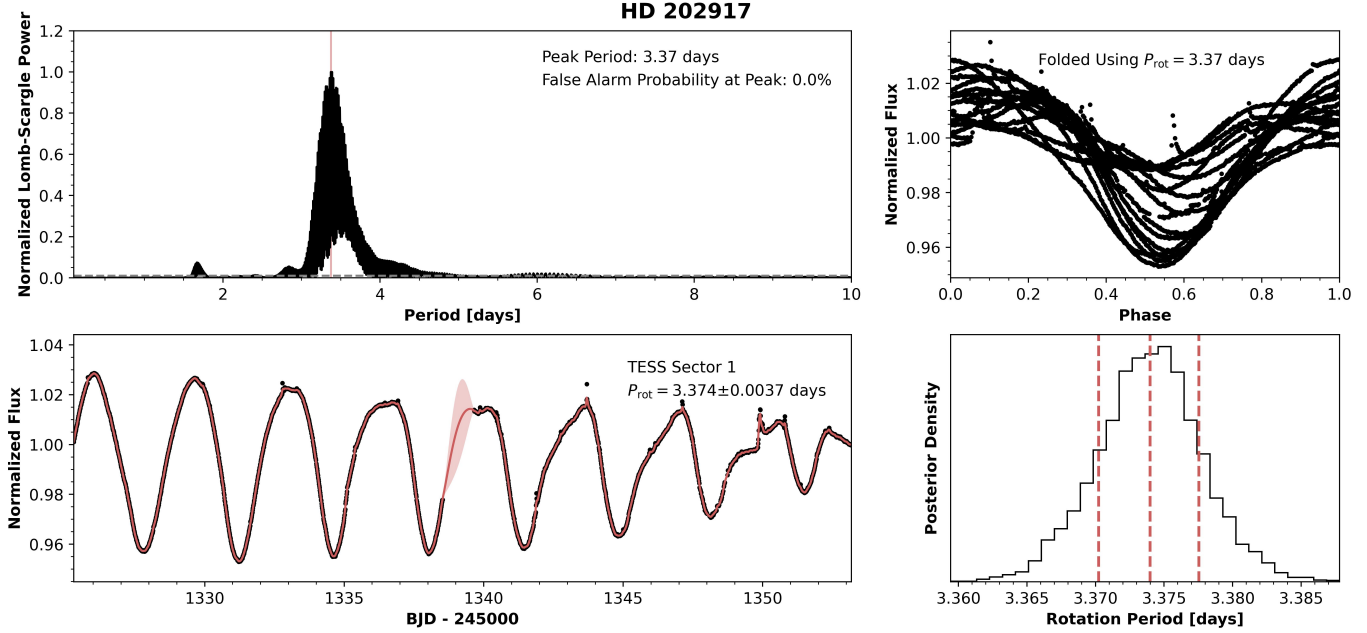


**Figure 12.** *Top left:* The Lomb-Scargle periodogram for the HD 202917 *TESS* PDCSAP light curve is shown in black. The dashed grey line marks the 1% FAP level while the shaded red region denotes the  $1\sigma$  confidence interval for the rotation period posterior. *Top right:* The phase-folded light curve using the peak period from the Lomb-Scargle periodogram. *Bottom left:* The black points show data from *TESS* Sector 1 while the red line and shaded region mark the mean and  $1\sigma$  confidence interval for the GP model. *Bottom right:* The histogram shows the rotation period posterior derived from the GP model while the dash red lines mark the median and  $1\sigma$  interval.

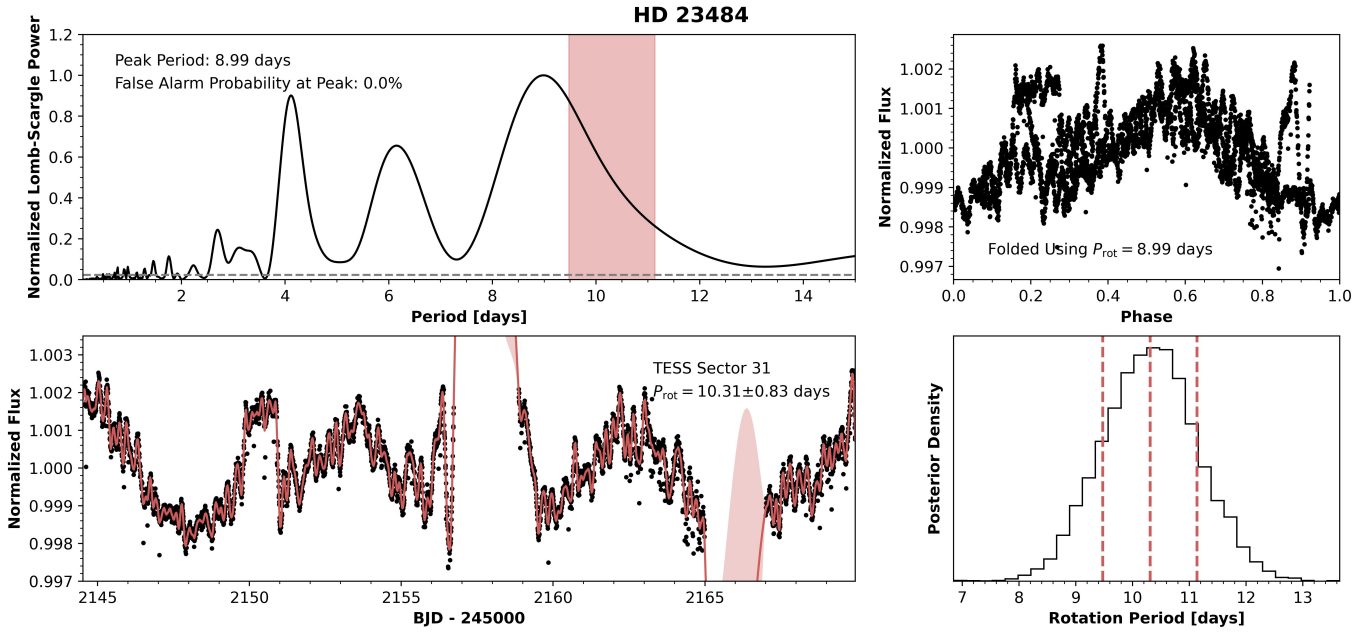


**Figure 13.** *Top left:* The Lomb-Scargle periodogram for the HD 23484 *TESS* PDCSAP light curve is shown in black. The dashed grey line marks the 1% FAP level while the shaded red region denotes the  $1\sigma$  confidence interval for the rotation period posterior. *Top right:* The phase-folded light curve using the peak period from the Lomb-Scargle periodogram. *Bottom left:* The black points show data from *TESS* Sector 31 while the red line and shaded region mark the mean and  $1\sigma$  confidence interval for the GP model. *Bottom right:* The histogram shows the rotation period posterior derived from the GP model while the dash red lines mark the median and  $1\sigma$  interval.

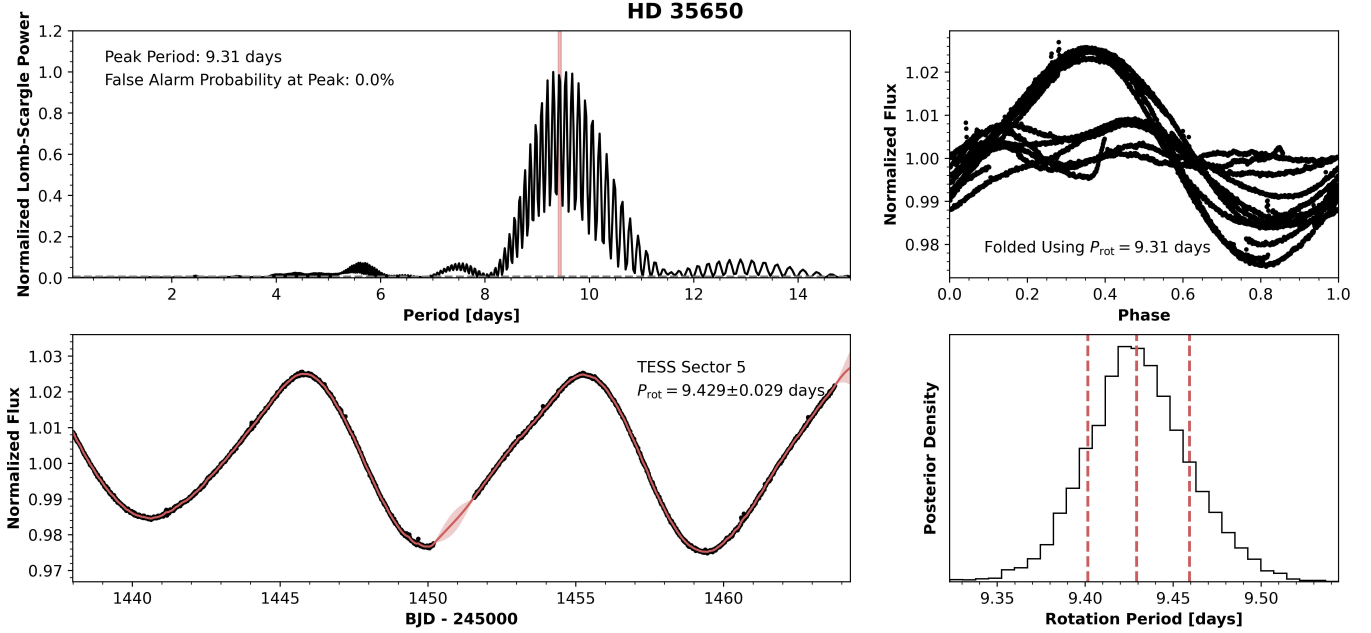


**Figure 14.** *Top left:* The Lomb-Scargle periodogram for the HD 35650 *TESS* PDCSAP light curve is shown in black. The dashed grey line marks the 1% FAP level while the shaded red region denotes the  $1\sigma$  confidence interval for the rotation period posterior. *Top right:* The phase-folded light curve using the peak period from the Lomb-Scargle periodogram. *Bottom left:* The black points show data from *TESS* Sector 5 while the red line and shaded region mark the mean and  $1\sigma$  confidence interval for the GP model. *Bottom right:* The histogram shows the rotation period posterior derived from the GP model while the dash red lines mark the median and  $1\sigma$  interval.

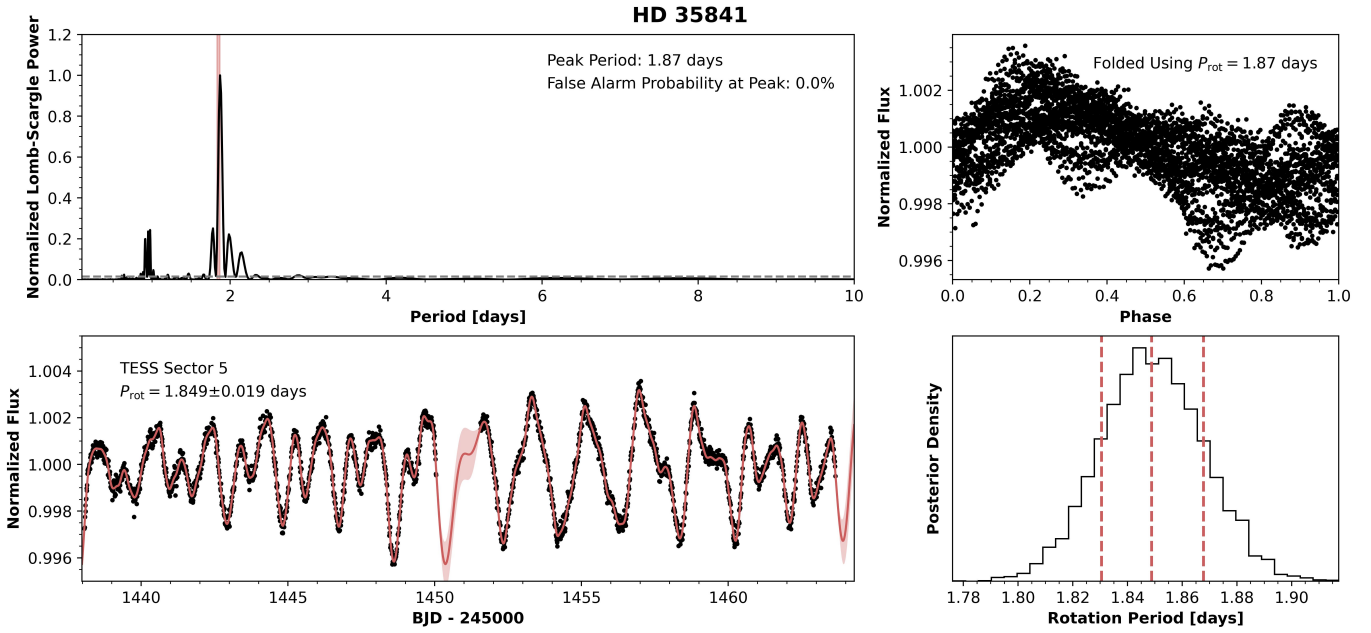


**Figure 15.** *Top left:* The Lomb-Scargle periodogram for the HD 35841 *TESS* PDCSAP light curve is shown in black. The dashed grey line marks the 1% FAP level while the shaded red region denotes the  $1\sigma$  confidence interval for the rotation period posterior. *Top right:* The phase-folded light curve using the peak period from the Lomb-Scargle periodogram. *Bottom left:* The black points show data from *TESS* Sector 5 while the red line and shaded region mark the mean and  $1\sigma$  confidence interval for the GP model. *Bottom right:* The histogram shows the rotation period posterior derived from the GP model while the dash red lines mark the median and  $1\sigma$  interval.

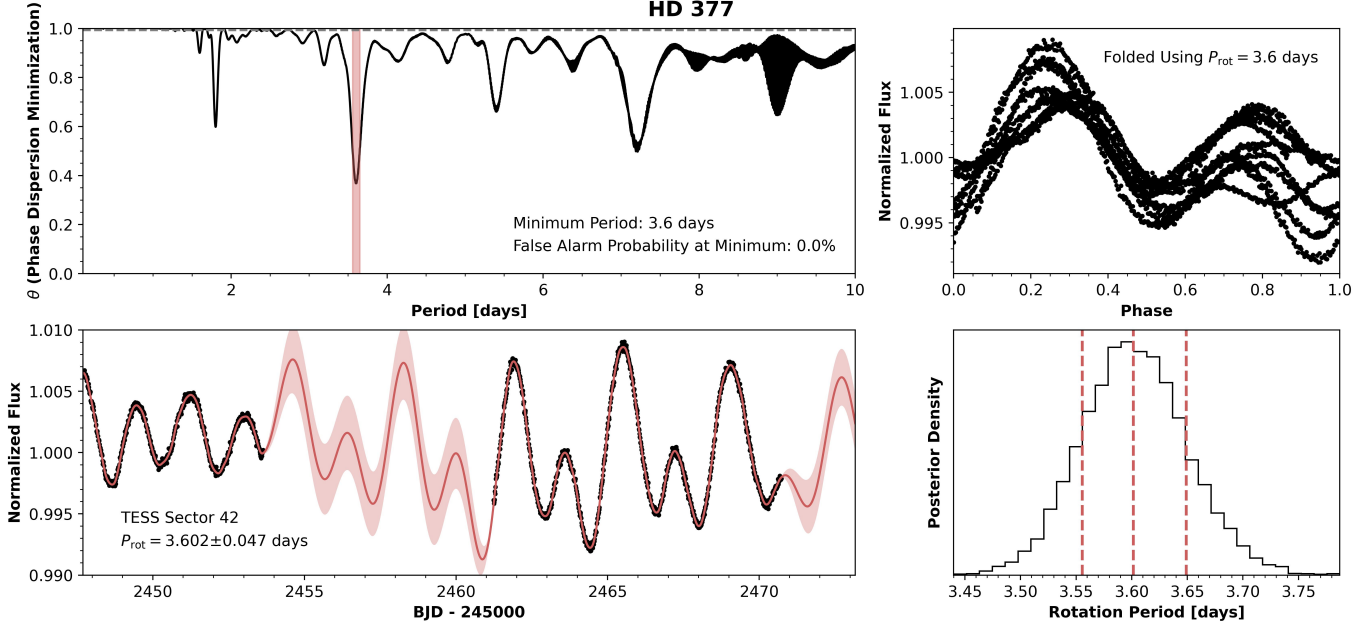


**Figure 16.** *Top left:* The phase dispersion minimization periodogram for the HD 377 *TESS* PDCSAP light curve is shown in black. The dashed grey line marks the 1% FAP level while the shaded red region denotes the  $1\sigma$  confidence interval for the rotation period posterior. *Top right:* The phase-folded light curve using the peak period from the Lomb-Scargle periodogram. *Bottom left:* The black points show data from *TESS* Sector 5 while the red line and shaded region mark the mean and  $1\sigma$  confidence interval for the GP model. *Bottom right:* The histogram shows the rotation period posterior derived from the GP model while the dash red lines mark the median and  $1\sigma$  interval.

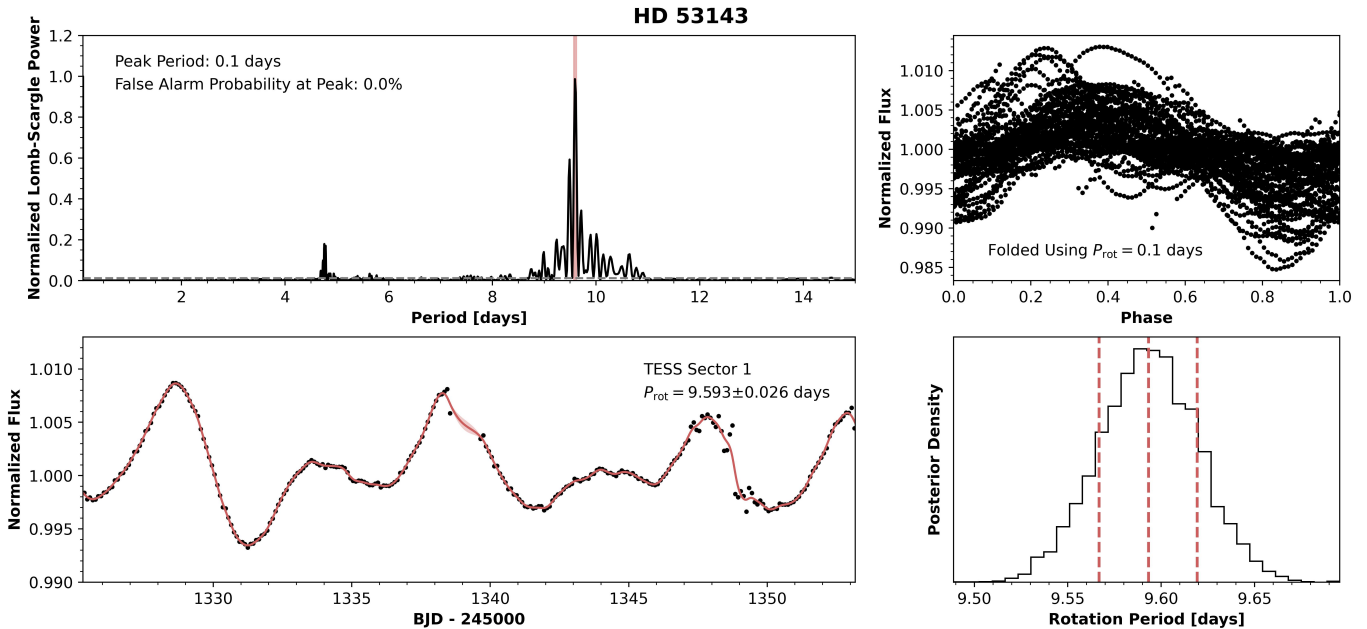


**Figure 17.** *Top left:* The Lomb-Scargle periodogram for the HD 53143 *TESS* PDCSAP light curve is shown in black. The dashed grey line marks the 1% FAP level while the shaded red region denotes the  $1\sigma$  confidence interval for the rotation period posterior. *Top right:* The phase-folded light curve using the peak period from the Lomb-Scargle periodogram. *Bottom left:* The black points show data from *TESS* Sector 1 while the red line and shaded region mark the mean and  $1\sigma$  confidence interval for the GP model. *Bottom right:* The histogram shows the rotation period posterior derived from the GP model while the dash red lines mark the median and  $1\sigma$  interval.

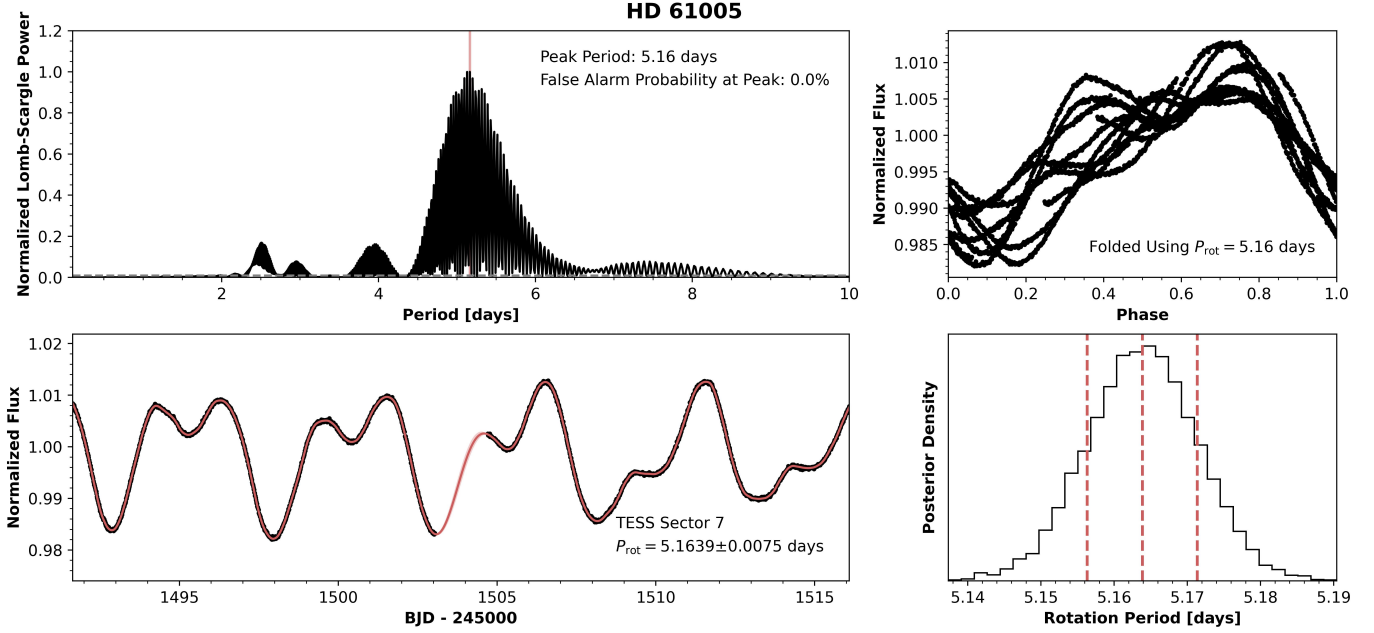


**Figure 18.** *Top left:* The Lomb-Scargle periodogram for the HD 61005 *TESS* PDCSAP light curve is shown in black. The dashed grey line marks the 1% FAP level while the shaded red region denotes the  $1\sigma$  confidence interval for the rotation period posterior. *Top right:* The phase-folded light curve using the peak period from the Lomb-Scargle periodogram. *Bottom left:* The black points show data from *TESS* Sector 7 while the red line and shaded region mark the mean and  $1\sigma$  confidence interval for the GP model. *Bottom right:* The histogram shows the rotation period posterior derived from the GP model while the dash red lines mark the median and  $1\sigma$  interval.

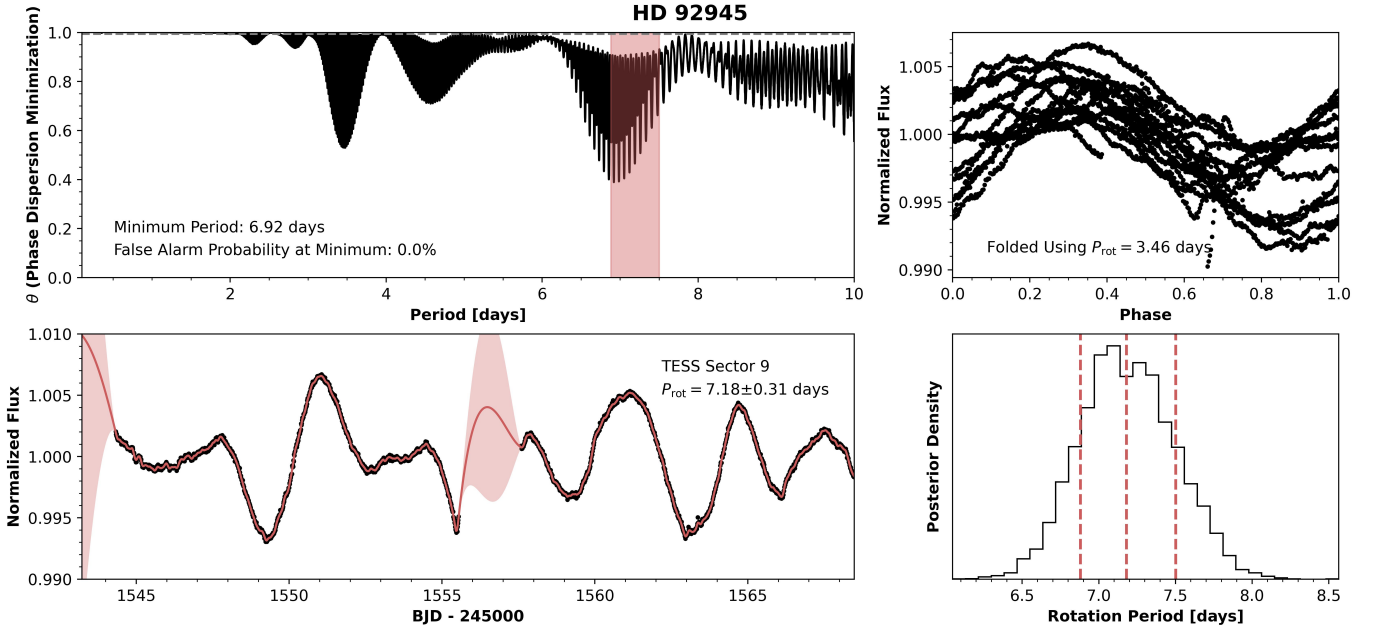


**Figure 19.** *Top left:* The phase dispersion minimization periodogram for the HD 92945 *TESS* PDCSAP light curve is shown in black. The dashed grey line marks the 1% FAP level while the shaded red region denotes the  $1\sigma$  confidence interval for the rotation period posterior. *Top right:* The phase-folded light curve using the peak period from the Lomb-Scargle periodogram. *Bottom left:* The black points show data from *TESS* Sector 9 while the red line and shaded region mark the mean and  $1\sigma$  confidence interval for the GP model. *Bottom right:* The histogram shows the rotation period posterior derived from the GP model while the dash red lines mark the median and  $1\sigma$  interval.

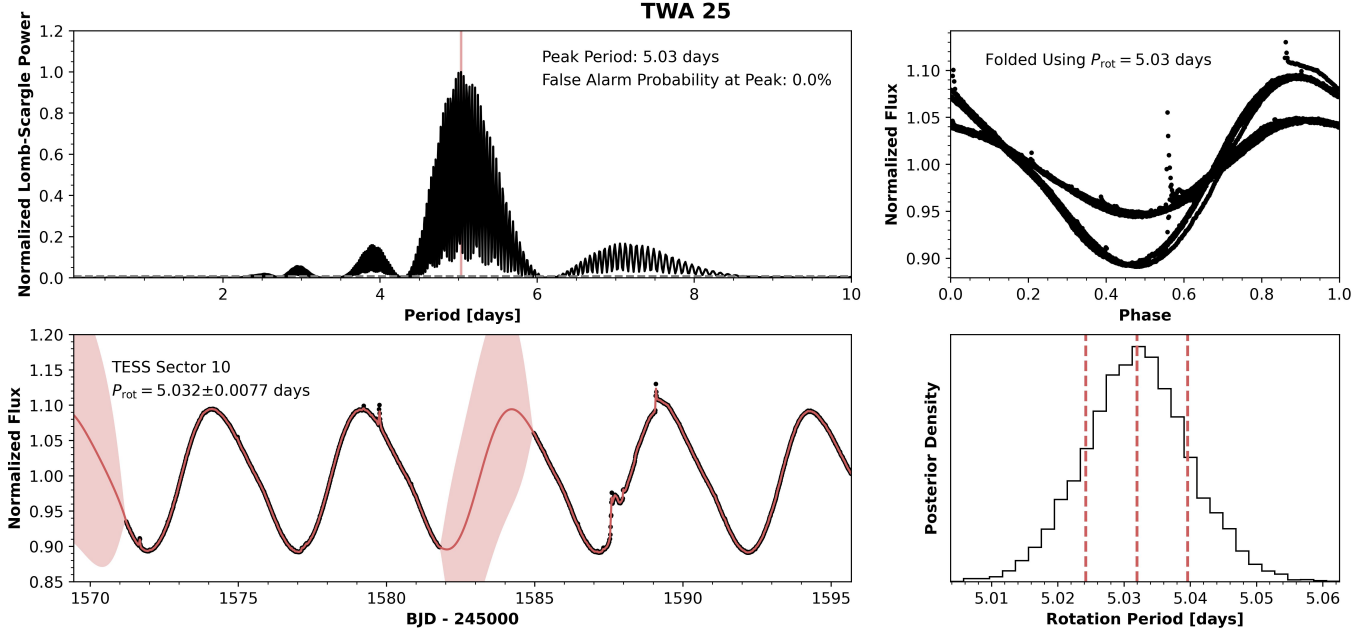


**Figure 20.** *Top left:* The Lomb-Scargle periodogram for the TWA 25 *TESS* PDCSAP light curve is shown in black. The dashed grey line marks the 1% FAP level while the shaded red region denotes the  $1\sigma$  confidence interval for the rotation period posterior. *Top right:* The phase-folded light curve using the peak period from the Lomb-Scargle periodogram. *Bottom left:* The black points show data from *TESS* Sector 10 while the red line and shaded region mark the mean and  $1\sigma$  confidence interval for the GP model. *Bottom right:* The histogram shows the rotation period posterior derived from the GP model while the dash red lines mark the median and  $1\sigma$  interval.

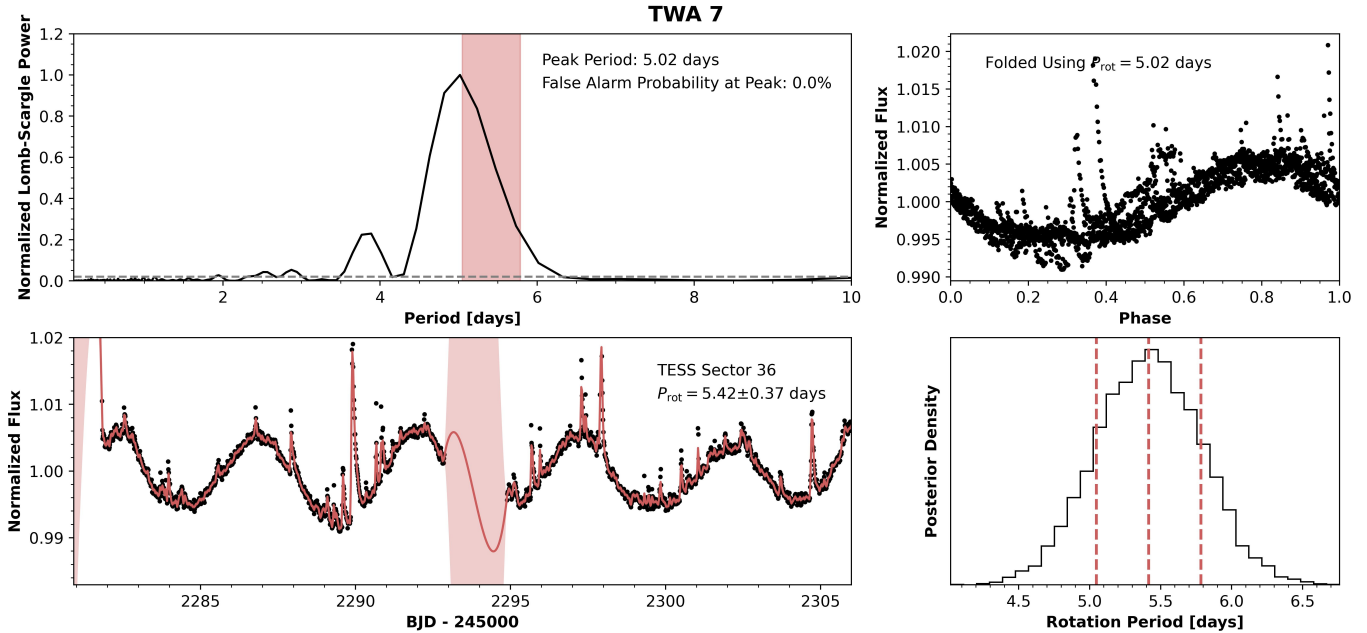


**Figure 21.** *Top left:* The Lomb-Scargle periodogram for the TWA 7 *TESS* PDCSAP light curve is shown in black. The dashed grey line marks the 1% FAP level while the shaded red region denotes the  $1\sigma$  confidence interval for the rotation period posterior. *Top right:* The phase-folded light curve using the peak period from the Lomb-Scargle periodogram. *Bottom left:* The black points show data from *TESS* Sector 36 while the red line and shaded region mark the mean and  $1\sigma$  confidence interval for the GP model. *Bottom right:* The histogram shows the rotation period posterior derived from the GP model while the dash red lines mark the median and  $1\sigma$  interval.

## REFERENCES

- Addison, B. C., Horner, J., Wittenmyer, R. A., et al. 2021, AJ, 162, 137, doi: [10.3847/1538-3881/ac1685](https://doi.org/10.3847/1538-3881/ac1685)
- Ahlers, J. P., Johnson, M. C., Stassun, K. G., et al. 2020, AJ, 160, 4, doi: [10.3847/1538-3881/ab8fa3](https://doi.org/10.3847/1538-3881/ab8fa3)
- Akeson, R. L., Ciardi, D. R., Millan-Gabet, R., et al. 2009, ApJ, 691, 1896, doi: [10.1088/0004-637X/691/2/1896](https://doi.org/10.1088/0004-637X/691/2/1896)
- Albrecht, S., Reffert, S., Snellen, I., Quirrenbach, A., & Mitchell, D. S. 2007, A&A, 474, 565, doi: [10.1051/0004-6361:20077953](https://doi.org/10.1051/0004-6361:20077953)
- Albrecht, S. H., Dawson, R. I., & Winn, J. N. 2022, PASP, 134, 082001, doi: [10.1088/1538-3873/ac6c09](https://doi.org/10.1088/1538-3873/ac6c09)
- Astropy Collaboration, Price-Whelan, A. M., SipHocz, B. M., et al. 2018, AJ, 156, 123, doi: [10.3847/1538-3881/aabc4f](https://doi.org/10.3847/1538-3881/aabc4f)
- Baliunas, S., Sokoloff, D., & Soon, W. 1996, ApJL, 457, L99, doi: [10.1086/309891](https://doi.org/10.1086/309891)
- Barnes, J. W. 2009, ApJ, 705, 683, doi: [10.1088/0004-637X/705/1/683](https://doi.org/10.1088/0004-637X/705/1/683)
- Basri, G., & Nguyen, H. T. 2018, ApJ, 863, 190, doi: [10.3847/1538-4357/aad3b6](https://doi.org/10.3847/1538-4357/aad3b6)
- Bate, M. R. 2018, MNRAS, 475, 5618, doi: [10.1093/mnras/sty169](https://doi.org/10.1093/mnras/sty169)
- Bate, M. R., Lodato, G., & Pringle, J. E. 2010, MNRAS, 401, 1505, doi: [10.1111/j.1365-2966.2009.15773.x](https://doi.org/10.1111/j.1365-2966.2009.15773.x)
- Batygin, K. 2012, Nature, 491, 418, doi: [10.1038/nature11560](https://doi.org/10.1038/nature11560)
- Batygin, K., Bodenheimer, P. H., & Laughlin, G. P. 2016, ApJ, 829, 114, doi: [10.3847/0004-637X/829/2/114](https://doi.org/10.3847/0004-637X/829/2/114)
- Beaugé, C., & Nesvorný, D. 2012, ApJ, 751, 119, doi: [10.1088/0004-637X/751/2/119](https://doi.org/10.1088/0004-637X/751/2/119)
- Beck, J. G., & Giles, P. 2005, ApJ, 621, L153, doi: [10.1086/429224](https://doi.org/10.1086/429224)
- Bell, C. P. M., Mamajek, E. E., & Naylor, T. 2015, MNRAS, 454, 593, doi: [10.1093/mnras/stv1981](https://doi.org/10.1093/mnras/stv1981)
- Benedict, G. F. 2022, Research Notes of the American Astronomical Society, 6, 45, doi: [10.3847/2515-5172/ac5b6b](https://doi.org/10.3847/2515-5172/ac5b6b)
- Bidelman, W. P. 1985, ApJS, 59, 197, doi: [10.1086/191069](https://doi.org/10.1086/191069)
- Borderies, N., Goldreich, P., & Tremaine, S. 1984, ApJ, 284, 429, doi: [10.1086/162423](https://doi.org/10.1086/162423)
- Brewer, J. M., Fischer, D. A., Valenti, J. A., & Piskunov, N. 2016, ApJS, 225, 32, doi: [10.3847/0067-0049/225/2/32](https://doi.org/10.3847/0067-0049/225/2/32)
- Chen, C. H., Mamajek, E. E., Bitner, M. A., et al. 2011, ApJ, 738, 122, doi: [10.1088/0004-637X/738/2/122](https://doi.org/10.1088/0004-637X/738/2/122)
- Choquet, É., Perrin, M. D., Chen, C. H., et al. 2016, ApJL, 817, L2, doi: [10.3847/2041-8205/817/1/L2](https://doi.org/10.3847/2041-8205/817/1/L2)
- Churcher, L. J., Wyatt, M. C., Duchêne, G., et al. 2011, MNRAS, 417, 1715, doi: [10.1111/j.1365-2966.2011.19341.x](https://doi.org/10.1111/j.1365-2966.2011.19341.x)
- Cutispoto, G., Pastori, L., Pasquini, L., et al. 2002, A&A, 384, 491, doi: [10.1051/0004-6361:20020040](https://doi.org/10.1051/0004-6361:20020040)
- Dahm, S. E., Slesnick, C. L., & White, R. J. 2012, ApJ, 745, 56, doi: [10.1088/0004-637X/745/1/56](https://doi.org/10.1088/0004-637X/745/1/56)
- Davies, C. L. 2019, MNRAS, 484, 1926, doi: [10.1093/mnras/stz086](https://doi.org/10.1093/mnras/stz086)
- Dawson, R. I., & Johnson, J. A. 2018, ARA&A, 56, 175, doi: [10.1146/annurev-astro-081817-051853](https://doi.org/10.1146/annurev-astro-081817-051853)
- Delorme, P., Schmidt, T., Bonnefoy, M., et al. 2017, A&A, 608, A79, doi: [10.1051/0004-6361/201731145](https://doi.org/10.1051/0004-6361/201731145)
- Desidera, S., Covino, E., Messina, S., et al. 2015, A&A, 573, A126, doi: [10.1051/0004-6361/201323168](https://doi.org/10.1051/0004-6361/201323168)
- Di Folco, E., Thévenin, F., Kervella, P., et al. 2004, A&A, 426, 601, doi: [10.1051/0004-6361:20047189](https://doi.org/10.1051/0004-6361:20047189)
- dos Santos, L. A., Meléndez, J., do Nascimento, J.-D., et al. 2016, A&A, 592, A156, doi: [10.1051/0004-6361/201628558](https://doi.org/10.1051/0004-6361/201628558)
- Ertel, S., Marshall, J. P., Augereau, J. C., et al. 2014, A&A, 561, A114, doi: [10.1051/0004-6361/201219945](https://doi.org/10.1051/0004-6361/201219945)
- Esposito, T. M., Duchêne, G., Kalas, P., et al. 2018, AJ, 156, 47, doi: [10.3847/1538-3881/aacbc9](https://doi.org/10.3847/1538-3881/aacbc9)
- Esposito, T. M., Kalas, P., Fitzgerald, M. P., et al. 2020, AJ, 160, 24, doi: [10.3847/1538-3881/ab9199](https://doi.org/10.3847/1538-3881/ab9199)
- Fabrycky, D. C., & Winn, J. N. 2009, ApJ, 696, 1230, doi: [10.1088/0004-637X/696/2/1230](https://doi.org/10.1088/0004-637X/696/2/1230)
- Faramaz, V., Krist, J., Stapelfeldt, K. R., et al. 2019, AJ, 158, 162, doi: [10.3847/1538-3881/ab3ec1](https://doi.org/10.3847/1538-3881/ab3ec1)
- Feng, F., Tuomi, M., Jones, H. R. A., et al. 2017, AJ, 154, 135, doi: [10.3847/1538-3881/aa83b4](https://doi.org/10.3847/1538-3881/aa83b4)
- Feng, F., Butler, R. P., Vogt, S. S., et al. 2022, ApJS, 262, 21, doi: [10.3847/1538-4365/ac7e57](https://doi.org/10.3847/1538-4365/ac7e57)
- Fielding, D. B., McKee, C. F., Socrates, A., Cunningham, A. J., & Klein, R. I. 2015, MNRAS, 450, 3306, doi: [10.1093/mnras/stv836](https://doi.org/10.1093/mnras/stv836)
- Foreman-Mackey, D. 2018, Research Notes of the American Astronomical Society, 2, 31, doi: [10.3847/2515-5172/aaaf6c](https://doi.org/10.3847/2515-5172/aaaf6c)
- Foreman-Mackey, D., Agol, E., Ambikasaran, S., & Angus, R. 2017, AJ, 154, 220, doi: [10.3847/1538-3881/aa9332](https://doi.org/10.3847/1538-3881/aa9332)
- Foreman-Mackey, D., Luger, R., Agol, E., et al. 2021, The Journal of Open Source Software, 6, 3285, doi: [10.21105/joss.03285](https://doi.org/10.21105/joss.03285)
- Foucart, F., & Lai, D. 2011, MNRAS, 412, 2799, doi: [10.1111/j.1365-2966.2010.18176.x](https://doi.org/10.1111/j.1365-2966.2010.18176.x)
- Giguere, M. J., Fischer, D. A., Zhang, C. X. Y., et al. 2016, ApJ, 824, 150, doi: [10.3847/0004-637X/824/2/150](https://doi.org/10.3847/0004-637X/824/2/150)

- Głębocki, R., & Gnaciński, P. 2005, in ESA Special Publication, Vol. 560, 13th Cambridge Workshop on Cool Stars, Stellar Systems and the Sun, ed. F. Favata, G. A. J. Hussain, & B. Battrick, 571
- Gray, R. O., Corbally, C. J., Garrison, R. F., et al. 2006, AJ, 132, 161, doi: [10.1086/504637](https://doi.org/10.1086/504637)
- Gray, R. O., Corbally, C. J., Garrison, R. F., McFadden, M. T., & Robinson, P. E. 2003, AJ, 126, 2048, doi: [10.1086/378365](https://doi.org/10.1086/378365)
- Greaves, J. S., Kennedy, G. M., Thureau, N., et al. 2014, MNRAS, 438, L31, doi: [10.1093/mnrasl/slt153](https://doi.org/10.1093/mnrasl/slt153)
- Hales, A. S., Gorti, U., Carpenter, J. M., Hughes, M., & Flaherty, K. 2019, ApJ, 878, 113, doi: [10.3847/1538-4357/ab211e](https://doi.org/10.3847/1538-4357/ab211e)
- Harlan, E. A., & Taylor, D. C. 1970, AJ, 75, 507, doi: [10.1086/110986](https://doi.org/10.1086/110986)
- Harris, C. R., Jarrod Millman, K., van der Walt, S. J., et al. 2020, Nature, 585, 357, doi: [10.1038/s41586-020-2649-2](https://doi.org/10.1038/s41586-020-2649-2)
- Haywood, R. D., Collier Cameron, A., Queloz, D., et al. 2014, MNRAS, 443, 2517, doi: [10.1093/mnras/stu1320](https://doi.org/10.1093/mnras/stu1320)
- Herczeg, G. J., & Hillenbrand, L. A. 2014, ApJ, 786, 97, doi: [10.1088/0004-637X/786/2/97](https://doi.org/10.1088/0004-637X/786/2/97)
- Hinkley, S., Lacour, S., Marleau, G. D., et al. 2022, arXiv e-prints, arXiv:2208.04867, doi: [10.48550/arXiv.2208.04867](https://doi.org/10.48550/arXiv.2208.04867)
- Hjorth, M., Albrecht, S., Hirano, T., et al. 2021, PNAS, 118, 2017418118, doi: [10.1073/pnas.2017418118](https://doi.org/10.1073/pnas.2017418118)
- Hojjatpanah, S., Figueira, P., Santos, N. C., et al. 2019, A&A, 629, A80, doi: [10.1051/0004-6361/201834729](https://doi.org/10.1051/0004-6361/201834729)
- Hom, J., Patience, J., Esposito, T. M., et al. 2020, AJ, 159, 31, doi: [10.3847/1538-3881/ab5af2](https://doi.org/10.3847/1538-3881/ab5af2)
- Houk, N. 1978, Michigan catalogue of two-dimensional spectral types for the HD stars  
—. 1982, Michigan Catalogue of Two-dimensional Spectral Types for the HD stars. Volume\_3. Declinations -40\_f0 to -26\_f0.
- Houk, N., & Cowley, A. P. 1975, University of Michigan Catalogue of two-dimensional spectral types for the HD stars. Volume I. Declinations -90\_ to -53\_f0.
- Houk, N., & Smith-Moore, M. 1988, Michigan Catalogue of Two-dimensional Spectral Types for the HD Stars. Volume 4, Declinations -26°.0 to -12°.0., Vol. 4
- Hunter, J. D. 2007, CSE, 9, 90, doi: [10.1109/MCSE.2007.55](https://doi.org/10.1109/MCSE.2007.55)
- Hurt, S. A., Quinn, S. N., Latham, D. W., et al. 2021, AJ, 161, 157, doi: [10.3847/1538-3881/abdec8](https://doi.org/10.3847/1538-3881/abdec8)
- Isaacson, H., & Fischer, D. 2010, ApJ, 725, 875, doi: [10.1088/0004-637X/725/1/875](https://doi.org/10.1088/0004-637X/725/1/875)
- Kahraman Aliçavuş, F., Niemczura, E., De Cat, P., et al. 2016, MNRAS, 458, 2307, doi: [10.1093/mnras/stw393](https://doi.org/10.1093/mnras/stw393)
- Keenan, P. C., & McNeil, R. C. 1989, ApJS, 71, 245, doi: [10.1086/191373](https://doi.org/10.1086/191373)
- Koen, C., Balona, L. A., Khadaroo, K., et al. 2003, MNRAS, 344, 1250, doi: [10.1046/j.1365-8711.2003.06912.x](https://doi.org/10.1046/j.1365-8711.2003.06912.x)
- Kraft, R. P. 1967, ApJ, 150, 551, doi: [10.1086/149359](https://doi.org/10.1086/149359)
- Lai, D., Foucart, F., & Lin, D. N. C. 2011, MNRAS, 412, 2790, doi: [10.1111/j.1365-2966.2010.18127.x](https://doi.org/10.1111/j.1365-2966.2010.18127.x)
- Lawler, S. M., Di Francesco, J., Kennedy, G. M., et al. 2014, MNRAS, 444, 2665, doi: [10.1093/mnras/stu1641](https://doi.org/10.1093/mnras/stu1641)
- Le Bouquin, J. B., Absil, O., Benisty, M., et al. 2009, A&A, 498, L41, doi: [10.1051/0004-6361/200911854](https://doi.org/10.1051/0004-6361/200911854)
- Lesage, A. L., & Wiedemann, G. 2014, A&A, 563, A86, doi: [10.1051/0004-6361/201322964](https://doi.org/10.1051/0004-6361/201322964)
- Lestrade, J. F., Matthews, B. C., Sibthorpe, B., et al. 2012, A&A, 548, A86, doi: [10.1051/0004-6361/201220325](https://doi.org/10.1051/0004-6361/201220325)
- Liseau, R., Eiroa, C., Fedele, D., et al. 2010, A&A, 518, L132, doi: [10.1051/0004-6361/201014601](https://doi.org/10.1051/0004-6361/201014601)
- Llop-Sayson, J., Wang, J. J., Ruffio, J.-B., et al. 2021, AJ, 162, 181, doi: [10.3847/1538-3881/ac134a](https://doi.org/10.3847/1538-3881/ac134a)
- Lubow, S. H., & Ogilvie, G. I. 2000, ApJ, 538, 326, doi: [10.1086/309101](https://doi.org/10.1086/309101)
- MacGregor, M. A., Wilner, D. J., Andrews, S. M., Lestrade, J.-F., & Maddison, S. 2015, ApJ, 809, 47, doi: [10.1088/0004-637X/809/1/47](https://doi.org/10.1088/0004-637X/809/1/47)
- MacGregor, M. A., Weinberger, A. J., Hughes, A. M., et al. 2018, ApJ, 869, 75, doi: [10.3847/1538-4357/aaec71](https://doi.org/10.3847/1538-4357/aaec71)
- MacGregor, M. A., Hurt, S. A., Stark, C. C., et al. 2022, ApJL, 933, L1, doi: [10.3847/2041-8213/ac7729](https://doi.org/10.3847/2041-8213/ac7729)
- Malmberg, D., Davies, M. B., & Heggie, D. C. 2011, MNRAS, 411, 859, doi: [10.1111/j.1365-2966.2010.17730.x](https://doi.org/10.1111/j.1365-2966.2010.17730.x)
- Malo, L., Artigau, É., Doyon, R., et al. 2014, ApJ, 788, 81, doi: [10.1088/0004-637X/788/1/81](https://doi.org/10.1088/0004-637X/788/1/81)
- Mamajek, E. E., & Hillenbrand, L. A. 2008, ApJ, 687, 1264, doi: [10.1086/591785](https://doi.org/10.1086/591785)
- Marino, S., Yelverton, B., Booth, M., et al. 2019, MNRAS, 484, 1257, doi: [10.1093/mnras/stz049](https://doi.org/10.1093/mnras/stz049)
- Marino, S., Zurlo, A., Faramaz, V., et al. 2020, MNRAS, 498, 1319, doi: [10.1093/mnras/staa2386](https://doi.org/10.1093/mnras/staa2386)
- Marmier, M., Ségransan, D., Udry, S., et al. 2013, A&A, 551, A90, doi: [10.1051/0004-6361/201219639](https://doi.org/10.1051/0004-6361/201219639)
- Marsden, S. C., Petit, P., Jeffers, S. V., et al. 2014, MNRAS, 444, 3517, doi: [10.1093/mnras/stu1663](https://doi.org/10.1093/mnras/stu1663)
- Martoli, E., Hébrard, G., Correia, A. C. M., Laskar, J., & Lecavelier des Etangs, A. 2021, A&A, 649, A177, doi: [10.1051/0004-6361/202040235](https://doi.org/10.1051/0004-6361/202040235)
- Masuda, K., & Winn, J. N. 2020, AJ, 159, 81, doi: [10.3847/1538-3881/ab65be](https://doi.org/10.3847/1538-3881/ab65be)
- Matrà, L., Dent, W. R. F., Wilner, D. J., et al. 2020, ApJ, 898, 146, doi: [10.3847/1538-4357/aba0a4](https://doi.org/10.3847/1538-4357/aba0a4)

- Matsakos, T., & Königl, A. 2017, AJ, 153, 60, doi: [10.3847/1538-3881/153/2/60](https://doi.org/10.3847/1538-3881/153/2/60)
- Matthews, E., Hinkley, S., Vigan, A., et al. 2017, ApJL, 843, L12, doi: [10.3847/2041-8213/aa7943](https://doi.org/10.3847/2041-8213/aa7943)
- Monnier, J. D., Che, X., Zhao, M., et al. 2012, ApJL, 761, L3, doi: [10.1088/2041-8205/761/1/L3](https://doi.org/10.1088/2041-8205/761/1/L3)
- Moore, N. W. H., Li, G., & Adams, F. C. 2020, ApJ, 901, 92, doi: [10.3847/1538-4357/abb08f](https://doi.org/10.3847/1538-4357/abb08f)
- Morales, F. Y., Bryden, G., Werner, M. W., & Stapelfeldt, K. R. 2016, ApJ, 831, 97, doi: [10.3847/0004-637X/831/1/97](https://doi.org/10.3847/0004-637X/831/1/97)
- Naoz, S. 2016, ARA&A, 54, 441, doi: [10.1146/annurev-astro-081915-023315](https://doi.org/10.1146/annurev-astro-081915-023315)
- NASA Exoplanet Archive. 2019, Confirmed Planets Table, IPAC, doi: [10.26133/NEA1](https://doi.org/10.26133/NEA1)
- Nielsen, E. L., De Rosa, R. J., Macintosh, B., et al. 2019, AJ, 158, 13, doi: [10.3847/1538-3881/ab16e9](https://doi.org/10.3847/1538-3881/ab16e9)
- Noyes, R. W., Hartmann, L. W., Baliunas, S. L., Duncan, D. K., & Vaughan, A. H. 1984, ApJ, 279, 763, doi: [10.1086/161945](https://doi.org/10.1086/161945)
- Oelkers, R. J., Rodriguez, J. E., Stassun, K. G., et al. 2018, AJ, 155, 39, doi: [10.3847/1538-3881/aa9bf4](https://doi.org/10.3847/1538-3881/aa9bf4)
- Paegert, M., Stassun, K. G., Collins, K. A., et al. 2021, arXiv e-prints, arXiv:2108.04778. <https://arxiv.org/abs/2108.04778>
- Pecaut, M. J., & Mamajek, E. E. 2016, MNRAS, 461, 794, doi: [10.1093/mnras/stw1300](https://doi.org/10.1093/mnras/stw1300)
- Petrovich, C., Muñoz, D. J., Kratter, K. M., & Malhotra, R. 2020, ApJ, 902, L5, doi: [10.3847/2041-8213/abb952](https://doi.org/10.3847/2041-8213/abb952)
- Plavchan, P., Werner, M. W., Chen, C. H., et al. 2009, ApJ, 698, 1068, doi: [10.1088/0004-637X/698/2/1068](https://doi.org/10.1088/0004-637X/698/2/1068)
- Plavchan, P., Barclay, T., Gagné, J., et al. 2020, Nature, 582, 497, doi: [10.1038/s41586-020-2400-z](https://doi.org/10.1038/s41586-020-2400-z)
- Queloz, D., Eggenberger, A., Mayor, M., et al. 2000, A&A, 359, L13, doi: [10.48550/arXiv.astro-ph/0006213](https://doi.org/10.48550/arXiv.astro-ph/0006213)
- Rajpaul, V., Aigrain, S., Osborne, M. A., Reece, S., & Roberts, S. 2015, MNRAS, 452, 2269, doi: [10.1093/mnras/stv1428](https://doi.org/10.1093/mnras/stv1428)
- Reiners, A., & Schmitt, J. H. M. M. 2003, A&A, 398, 647, doi: [10.1051/0004-6361:20021642](https://doi.org/10.1051/0004-6361:20021642)
- Ren, B., Choquet, É., Perrin, M. D., et al. 2019, ApJ, 882, 64, doi: [10.3847/1538-4357/ab3403](https://doi.org/10.3847/1538-4357/ab3403)
- Rimoldini, L., Dubath, P., Süveges, M., et al. 2012, MNRAS, 427, 2917, doi: [10.1111/j.1365-2966.2012.21752.x](https://doi.org/10.1111/j.1365-2966.2012.21752.x)
- Robertson, P., Mahadevan, S., Endl, M., & Roy, A. 2014, Science, 345, 440, doi: [10.1126/science.1253253](https://doi.org/10.1126/science.1253253)
- Rodet, L., & Lai, D. 2022, MNRAS, 509, 1010, doi: [10.1093/mnras/stab3046](https://doi.org/10.1093/mnras/stab3046)
- Rogers, T. M., Lin, D. N. C., & Lau, H. H. B. 2012, ApJ, 758, L6, doi: [10.1088/2041-8205/758/1/L6](https://doi.org/10.1088/2041-8205/758/1/L6)
- Rogers, T. M., Lin, D. N. C., McElwaine, J. N., & Lau, H. H. B. 2013, ApJ, 772, 21, doi: [10.1088/0004-637X/772/1/21](https://doi.org/10.1088/0004-637X/772/1/21)
- Saar, S. H., & Osten, R. A. 1997, MNRAS, 284, 803, doi: [10.1093/mnras/284.4.803](https://doi.org/10.1093/mnras/284.4.803)
- Saffe, C., Miquelarena, P., Alacoria, J., et al. 2021, A&A, 647, A49, doi: [10.1051/0004-6361/202040132](https://doi.org/10.1051/0004-6361/202040132)
- Salvatier, J., Wiecki, T. V., & Fonnesbeck, C. 2016, PeerJ Computer Science, 2, e55
- Schlaufman, K. C. 2010, ApJ, 719, 602, doi: [10.1088/0004-637X/719/1/602](https://doi.org/10.1088/0004-637X/719/1/602)
- Schneider, G., Grady, C. A., Hines, D. C., et al. 2014, AJ, 148, 59, doi: [10.1088/0004-6256/148/4/59](https://doi.org/10.1088/0004-6256/148/4/59)
- Schneider, G., Grady, C. A., Stark, C. C., et al. 2016, AJ, 152, 64, doi: [10.3847/0004-6256/152/3/64](https://doi.org/10.3847/0004-6256/152/3/64)
- Shkolnik, E. L., Allers, K. N., Kraus, A. L., Liu, M. C., & Flagg, L. 2017, AJ, 154, 69, doi: [10.3847/1538-3881/aa77fa](https://doi.org/10.3847/1538-3881/aa77fa)
- Shporer, A., & Brown, T. 2011, ApJ, 733, 30, doi: [10.1088/0004-637X/733/1/30](https://doi.org/10.1088/0004-637X/733/1/30)
- Smith, J. C., Stumpe, M. C., Van Cleve, J. E., et al. 2012, PASP, 124, 1000, doi: [10.1086/667697](https://doi.org/10.1086/667697)
- Smith, R., Churcher, L. J., Wyatt, M. C., Moerchen, M. M., & Telesco, C. M. 2009, A&A, 493, 299, doi: [10.1051/0004-6361:200810706](https://doi.org/10.1051/0004-6361:200810706)
- Soto, M. G., & Jenkins, J. S. 2018, A&A, 615, A76, doi: [10.1051/0004-6361/201731533](https://doi.org/10.1051/0004-6361/201731533)
- Spalding, C., & Batygin, K. 2015, ApJ, 811, 82, doi: [10.1088/0004-637X/811/2/82](https://doi.org/10.1088/0004-637X/811/2/82)
- Stassun, K. G., Oelkers, R. J., Pepper, J., et al. 2018, AJ, 156, 102, doi: [10.3847/1538-3881/aad050](https://doi.org/10.3847/1538-3881/aad050)
- Stellingwerf, R. F. 1978, ApJ, 224, 953, doi: [10.1086/156444](https://doi.org/10.1086/156444)
- Stephenson, C. B. 1986, AJ, 92, 139, doi: [10.1086/114146](https://doi.org/10.1086/114146)
- Strassmeier, K., Washuettl, A., Granzer, T., Scheck, M., & Weber, M. 2000, A&AS, 142, 275, doi: [10.1051/aas:2000328](https://doi.org/10.1051/aas:2000328)
- Stumpe, M. C., Smith, J. C., Catanzarite, J. H., et al. 2014, PASP, 126, 100, doi: [10.1086/674989](https://doi.org/10.1086/674989)
- Stumpe, M. C., Smith, J. C., Van Cleve, J. E., et al. 2012, PASP, 124, 985, doi: [10.1086/667698](https://doi.org/10.1086/667698)
- Takaishi, D., Tsukamoto, Y., & Suto, Y. 2020, MNRAS, 492, 5641, doi: [10.1093/mnras/staa179](https://doi.org/10.1093/mnras/staa179)
- Thies, I., Kroupa, P., Goodwin, S. P., Stamatellos, D., & Whitworth, A. P. 2011, MNRAS, 417, 1817, doi: [10.1111/j.1365-2966.2011.19390.x](https://doi.org/10.1111/j.1365-2966.2011.19390.x)
- Torres, C. A. O., Quast, G. R., da Silva, L., et al. 2006, A&A, 460, 695, doi: [10.1051/0004-6361:20065602](https://doi.org/10.1051/0004-6361:20065602)

- Triaud, A. H. M. J. 2018, in *Handbook of Exoplanets*, ed. H. J. Deeg & J. A. Belmonte, 2,  
doi: [10.1007/978-3-319-55333-7\\_2](https://doi.org/10.1007/978-3-319-55333-7_2)
- Trifonov, T., Kürster, M., Zechmeister, M., et al. 2018, *A&A*, 609, A117, doi: [10.1051/0004-6361/201731442](https://doi.org/10.1051/0004-6361/201731442)
- Tristan, I., & Isella, A. 2019, in *American Astronomical Society Meeting Abstracts*, Vol. 233, American Astronomical Society Meeting Abstracts #233, 163.06
- van Belle, G. T., & von Braun, K. 2009, *ApJ*, 694, 1085,  
doi: [10.1088/0004-637X/694/2/1085](https://doi.org/10.1088/0004-637X/694/2/1085)
- Virtanen, P., Gommers, R., Oliphant, T. E., et al. 2020, *Nature Methods*, 17, 261, doi: [10.1038/s41592-019-0686-2](https://doi.org/10.1038/s41592-019-0686-2)
- Vogt, S. S., Wittenmyer, R. A., Butler, R. P., et al. 2010, *ApJ*, 708, 1366, doi: [10.1088/0004-637X/708/2/1366](https://doi.org/10.1088/0004-637X/708/2/1366)
- Watson, C. A., Littlefair, S. P., Diamond, C., et al. 2011, *MNRAS*, 413, L71, doi: [10.1111/j.1745-3933.2011.01036.x](https://doi.org/10.1111/j.1745-3933.2011.01036.x)
- Winn, J. N., Fabrycky, D., Albrecht, S., & Johnson, J. A. 2010, *ApJ*, 718, L145,  
doi: [10.1088/2041-8205/718/2/L145](https://doi.org/10.1088/2041-8205/718/2/L145)
- Winter, A. J., Kruijssen, J. M. D., Longmore, S. N., & Chevance, M. 2020, *Nature*, 586, 528,  
doi: [10.1038/s41586-020-2800-0](https://doi.org/10.1038/s41586-020-2800-0)
- Wyatt, M. C., Kennedy, G., Sibthorpe, B., et al. 2012, *MNRAS*, 424, 1206,  
doi: [10.1111/j.1365-2966.2012.21298.x](https://doi.org/10.1111/j.1365-2966.2012.21298.x)
- Yep, A. C., & White, R. J. 2022, *MNRAS*, 511, 4500,  
doi: [10.1093/mnras/stab3725](https://doi.org/10.1093/mnras/stab3725)
- Zakhzhay, O. V., Launhardt, R., Müller, A., et al. 2022, *A&A*, 667, A63, doi: [10.1051/0004-6361/202244213](https://doi.org/10.1051/0004-6361/202244213)
- Zanazzi, J. J., & Lai, D. 2018, *MNRAS*, 478, 835,  
doi: [10.1093/mnras/sty1075](https://doi.org/10.1093/mnras/sty1075)
- Zechmeister, M., & Kürster, M. 2009, *A&A*, 496, 577,  
doi: [10.1051/0004-6361:200811296](https://doi.org/10.1051/0004-6361:200811296)
- Zhou, G., Latham, D. W., Bieryla, A., et al. 2016, *MNRAS*, 460, 3376, doi: [10.1093/mnras/stw1107](https://doi.org/10.1093/mnras/stw1107)
- Zúñiga-Fernández, S., Bayo, A., Elliott, P., et al. 2021, *A&A*, 645, A30, doi: [10.1051/0004-6361/202037830](https://doi.org/10.1051/0004-6361/202037830)
- Zwintz, K., Reese, D. R., Neiner, C., et al. 2019, *A&A*, 627, A28, doi: [10.1051/0004-6361/201834744](https://doi.org/10.1051/0004-6361/201834744)